

Study of vector meson + baryon resonance production in π^+p interactions at 7.1 GeV/c

S. U. Chung and S. D. Protopopescu*

Brookhaven National Laboratory, Upton, New York 11973

R. L. Eisner†

Case Western Reserve University, Cleveland, Ohio 44106

S. M. Flatté

University of California, Santa Cruz, California 95064

(Received 11 March 1975)

From a large-statistics π^+p experiment at 7.1 GeV/c, data are presented on the reactions $\pi^+p \rightarrow \rho^0\Delta^{++}(1238)$ and $\pi^+p \rightarrow \omega\Delta^{++}(1238)$. Cross sections, differential cross sections, and vector-meson single-density-matrix elements are presented and a general comparison of the production properties of the two reactions is given. In addition to (ρ, ω) $\Delta^{++}(1238)$ production there is also strong evidence for production of a π^+p enhancement with mass ~ 1880 MeV, $\Gamma \sim 200$ MeV, and $J \geq \frac{7}{2}$ produced in association with the ρ and ω resonances. Detailed properties of this structure are presented and its production mechanism is compared with that of the corresponding $\Delta(1238)$ reactions. This state is also observed in the reaction $K^+p \rightarrow K^*(890)\Delta^{++}(1880)$ at 12.0 GeV/c, for which data are also presented.

I. INTRODUCTION

From a large sample of events of the final states

$$\pi^+p \rightarrow \pi^+\pi^-\pi^+p: 80\,000 \text{ events} \quad (1)$$

$$-\pi^+\pi^-\pi^0\pi^+p: 81\,000 \text{ events}, \quad (2)$$

at 7.1 GeV/c, data are presented on the quasi-two-body reactions

$$\pi^+p \rightarrow \rho^0\Delta^{++}(1238) \quad (3)$$

$$-\omega\Delta^{++}(1238). \quad (4)$$

A systematic analysis, from which the cross sections, differential cross sections, and vector-meson density-matrix elements are extracted, allows for a comparison of the production properties of the two reactions. The unnatural- and natural-parity exchange contributions are examined, and some general comments on the nature of the exchange mechanism are given.

In addition to the $\Delta^{++}(1238)$ + vector meson reactions, the analysis of (1) and (2) along with that of

$$K^+p \rightarrow K^+\pi^-\pi^+p: 29\,968 \text{ events} \quad (5)$$

at an incident K^+ momentum of 12 GeV/c yields evidence for a π^+p enhancement with mass ~ 1880 MeV and width ~ 200 MeV. This state is produced in association with the ρ , ω , and $K^*(890)$ resonances, respectively. An examination of the decay angular distribution reveals significant structure in the $H(LM) [\propto Y(LM)]$ moments up to $L = 6$, which implies that this broad structure can most readily be associated with the $J^P = \frac{7}{2}^+$

$\Delta^{++}(1950)$ found in πp phase-shift analyses. Its production properties are found to be very similar to, though not exactly the same as, those of the $\Delta^{++}(1238)$ produced in (3) and (4).

The data sample is discussed in Sec. II. The results of the extraction of the cross section, differential cross section, and vector-meson density-matrix elements are presented in Sec. III.

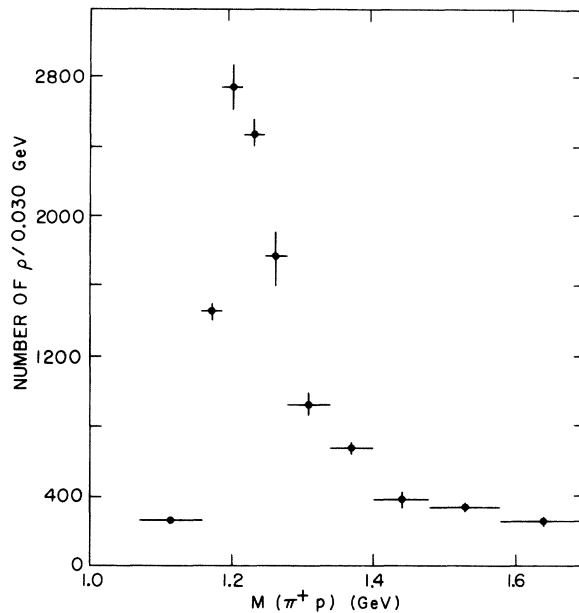


FIG. 1. Number of ρ events, plotted as a function $p\pi^+$ effective mass, from the reaction $\pi^+p \rightarrow \pi^+\pi^+\pi^-p$. The resulting fit to this mass spectrum, for the number of $\Delta^{++}(1238)$ events, allows for the extraction of the $\pi^+p \rightarrow \rho^0\Delta^{++}(1238)$ cross section.

In Sec. IV the production properties of reactions (3) and (4) are compared with current theoretical ideas on the nature of the exchange mechanism. In Sec. V the properties of the high-mass π^+p state are explored. Comparisons of $(\rho, \omega)\Delta^{++}(1880)$ with $(\rho, \omega)\Delta^{++}(1238)$ are given in Sec. VI. Section VII is reserved for summary and conclusions.

II. DATA SAMPLE

The data for the π^+p and K^+p samples are both derived from 700 000-picture exposures of the 82-inch hydrogen-filled bubble chamber at Stanford Linear Accelerator Center. They correspond, after appropriate corrections, to 38- and 32-event/ μb experiments, respectively. The event-selection criteria and other pertinent hypothesis-dependent details can be found in Ref. 1 [reaction (1)], Ref. 2 [reaction (2)], and Ref. 3 [reaction (5)].

III. PRODUCTION PROPERTIES

A. Cross-section determination

1. $\pi^+p \rightarrow \rho^0\Delta^{++}(1238)$

The number of $\rho\Delta^{++}$ events in reaction (1) was extracted using the slice technique of Aguilar-Benitez *et al.*⁴ For the present channel, following a $-t < 1.0 \text{ GeV}^2$ selection (where t is the square of the momentum transfer between target proton and outgoing $p\pi^+$ system), the method consisted of dividing the $p\pi^+$ effective mass spectrum into ten slices in the range

$$1.07 \leq M(p\pi^+) \leq 1.70 \text{ GeV}. \quad (6)$$

Fits were then performed on the corresponding $\pi^+\pi^-$ effective mass spectrum to a form with a P -wave ρ^0 Breit-Wigner shape multiplying phase space and a second-order polynomial in mass as representative of the background. The resonance mass and width were determined from an over-all fit to the $\pi^+\pi^-$ effective mass spectrum for events in the Δ^{++} region (6). Because of the distortion of the mass plot in the high-mass side of the ρ^0 due to the S^* effect it was not possible to fit these distributions with any simple polynomial form for the background.⁵ Therefore, we have chosen to fit essentially "half the ρ " region,

$$0.40 \leq M(\pi^+\pi^-) \leq 0.82 \text{ GeV},$$

and have corrected for the events in both the upper half and the tail of the ρ in the manner described below. The fits to the resultant $\pi^+\pi^-$ mass spectra, which were in excellent agreement with the experimental distributions,⁶ produced the results

displayed in Fig. 1, in which a large $\Delta^{++}(1238)$ signal is observed over a relatively small background. The spectrum shown in Fig. 1 was then fitted to a Δ^{++} Breit-Wigner shape multiplying phase space and a phase-space background. The number of resonance events so obtained represents the background-subtracted $\rho^0\Delta^{++}$ events in the fitted region. This number was then corrected (by a factor 1.93; see Ref. 7) to correspond to events in the ρ^0 tails including \pm four resonance widths. The resulting number of events is $23\,303 \pm 672$ in the mass region defined by

$$1.07 \leq M(p\pi^+) \leq 1.70 \text{ GeV},$$

$$M\rho - 4\Gamma\rho \leq M(\pi^+\pi^-) \leq M\rho + 4\Gamma\rho,$$

which corresponds to a cross section:

$$\sigma[\pi^+p \rightarrow \rho^0\Delta^{++}(1238)] = (613 \pm 25) \mu\text{b}.$$
⁸

2. $\pi^+p \rightarrow \omega\Delta^{++}(1238)$

The number of $\Delta^{++}\omega$ events in reaction (2) was, again, extracted through the use of the slice technique. The mass and width of the ω were determined from an over-all fit to the $\pi^+\pi^-\pi^0$ effective mass spectrum for events in the Δ^{++} region (6). A matrix element was used which included a Breit-Wigner shape for the ω plus a second-order polynomial background. The mass (0.780 GeV) and the effective width (0.025 GeV) of the ω were then fixed at the values determined from this fit, and each $\pi^+\pi^-\pi^0$ effective mass spectrum corresponding to ten π^+p mass slices was fitted to determine the resonance fraction in the region

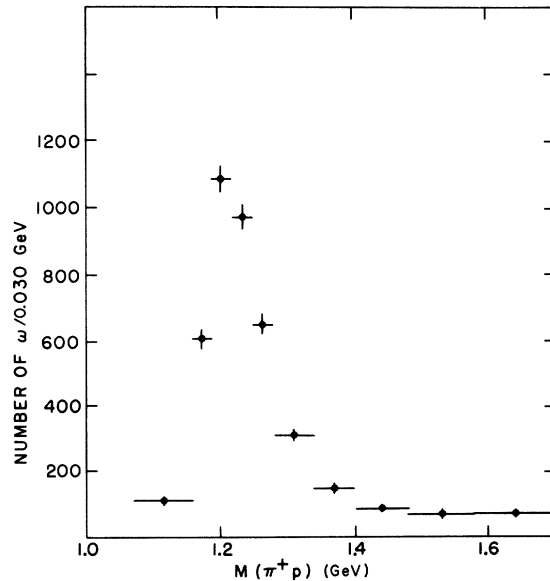


FIG. 2. Number of ω events, plotted as a function of $p\pi^+$ effective mass, from the reaction $\pi^+p \rightarrow \pi^+\pi^-\pi^0\pi^+p$.

$$0.68 \leq M(\pi^+ \pi^- \pi^0) \leq 0.88 \text{ GeV}.$$

The number of ω events so obtained in each $p\pi^+$ mass slice is shown in Fig. 2. The fit to this mass spectrum, in which a large $\Delta^{++}(1238)$ signal is observed, yields 4830 ± 107 events of reaction (4). After correction for the neutral/charged branching ratio⁹ of the ω , a cross section

$$\sigma[\pi^+ p \rightarrow \omega \Delta^{++}(1238)] = (140 \pm 3) \mu\text{b}$$

is obtained. (The quoted error is statistical.)

3. Comment on cross-section determination

Note that the $\rho\Delta^{++}$ and $\omega\Delta^{++}$ cross sections have both been obtained in the same interval of $p\pi^+$ mass and correspond to events included within the same number of resonance widths (i.e., 4Γ). Hence, the $\rho\Delta/\omega\Delta$ cross-section ratio and all comparisons dependent on the relative normalizations should be more reliable in the present work than in experiments in which the cross sections are extracted without regard to the intervals of mass spectrum used to determine the resonance fractions. Large discrepancies can result in cross-section determinations dependent upon the relative ratio of the fitted interval of the mass spectrum to the number of resonance widths. Clearly, in a comparison of cross sections it is absolutely essential that the ratio be made the same in all cases.

B. Differential cross section and density-matrix elements

1. Method of extraction

For both reactions (3) and (4), the mass-dependent partial-wave analysis proposed by Aguilar-Benitez *et al.*¹⁰ was employed to extract the number of resonance events and the vector-meson density-matrix elements as a function of momentum transfer. We briefly outline the method of analysis; more details are to be found in Ref. 10. This approach yields the resonance density-matrix elements free of the need for any substantial background corrections. In the case of the $\omega\Delta^{++}$ reaction, the method assumes that the background in the ω region has no angular dependences¹¹; for the $\Delta^{++}\rho^0$ the approach allows for a P -wave resonance, which may interfere with an S -wave background. The mass-dependent probability function can then be written, in both cases, as

$$\frac{d\sigma(\cos\theta, \phi)}{dm d\Omega} = \left. \frac{d\sigma}{dm d\Omega} \right|_{\text{background}} + \left. \frac{d\sigma}{dm d\Omega} \right|_{\text{resonance}}, \quad (7)$$

where the S -wave (or flat) background is paramet-

erized by

$$\left. \frac{d\sigma}{dm d\Omega} \right|_{\text{background}} = \frac{\epsilon_B^2 |f_B(m)|^2}{4\pi}$$

and the resonance mass and angular dependence by

$$\left. \frac{d\sigma}{dm d\Omega} \right|_{\text{resonance}} = \epsilon_R^2 |f_R(m)|^2 I_R(\Omega),$$

where ϵ_B^2 (ϵ_R^2) is the fraction of background (resonance) in the region over which the fit is performed, with $\epsilon_B^2 + \epsilon_R^2 = 1$. $|f_B(m)|^2$ ($|f_R(m)|^2$) is the background (resonance) mass dependence through the region of interest, and which in the present analysis is assumed to be linear in mass (assumed to have an energy-independent Breit-Wigner shape). Any small deviations from the assumed mass dependences have been found to have no significant effect on the values of the resonance density-matrix elements. For the analysis of the $(\pi^+ \pi^-)\Delta^{++}(1238)$ the method explicitly assumes that the so-called ϵ^0 effect does not produce a large bump under the ρ^0 resonance; this assumption is in agreement with the results of the $\pi\pi$ phase shifts obtained in this channel.¹ In the above,

$$I_R(\Omega) = \frac{1}{4\pi} \left[1 + \sum_{M=0}^2 H_R(2M) B_M^2(\Omega) \right],$$

where $\Omega = (\cos\theta, \phi)$ represents the usual Jackson (J) or helicity (H) frame angles and $B_M^2(\Omega) = (2 - \delta_{M0}) \times 5 d_{M0}^2(\theta) \cos M\phi$. The $H_R(2M)$ moments are related to the usual P -wave density-matrix elements, $\rho_{mm'}$, as follows:

$$\rho_{00} = \frac{1}{3} [1 + 5H_R(20)],$$

$$\rho_{1-1} = -\frac{5}{\sqrt{6}} H_R(22),$$

$$\rho_{11} = \frac{1}{3} [1 - \frac{5}{2} H_R(20)],$$

$$\text{Re}\rho_{10} = \frac{5}{2\sqrt{3}} H_R(21).$$

Maximum-likelihood fits to the form (7) were performed on the events selected to have

$$1.14 \leq M(\pi^+ p) \leq 1.34 \text{ GeV}$$

and

$$0.40 \leq M(\pi^+ \pi^-) \leq 1.0 \text{ GeV, reaction (3),}$$

$$0.68 \leq M(\pi^+ \pi^- \pi^0) \leq 0.88 \text{ GeV, reaction (4),}$$

and the $\rho_{mm'}$ and ϵ_R^2 were extracted as a function of momentum transfer. We reserve for discussion until Sec. III B 3 a description of the resultant $\rho_{mm'}$ distributions; we now proceed to describe the $d\sigma/dt$.

With ϵ_R^2 in a bin of $-t$ and the corresponding total number of events N_T , the number of ρ (ω)

events is simply $\epsilon_R^2 N_T$. The background from the process $\pi^+ p \rightarrow \rho^0 \pi^+ p$ ($\pi^+ p \rightarrow \omega \pi^+ p$) is small in the narrow $p\pi^+$ interval defined above [see Fig. 1 (2)] and, as such, should have little effect on the extracted $\rho\Delta^{++}$ ($\omega\Delta^{++}$) production angular distribution. Therefore, the distribution of $\epsilon_R^2 N_T$ as a function of $-t$ should be proportional to the $d\sigma/dt$ of the $\rho\Delta^{++}$ ($\omega\Delta^{++}$) reaction. The number of events in the $\rho\Delta^{++}$ ($\omega\Delta^{++}$) region is given in Table I and the fraction obtained from the maximum-likelihood fits in Table II (III). The number of $\rho\Delta^{++}$ ($\omega\Delta^{++}$) events was normalized to the total reaction cross section, as obtained from the slice technique described above, so that

$$\int \epsilon_R^2(-t) N_T(-t) dt = \sigma E,$$

where the integral extends over all $|t| < 1.0 \text{ GeV}^2$, and the conversion factor E was determined. The value of the differential cross section in each bin of momentum transfer is then

$$\frac{d\sigma}{dt} = \frac{\epsilon_R^2 N_T}{E \Delta t}.$$

The values of $d\sigma/dt$ so obtained are given in Table I.

2. Description of $d\sigma/dt$

a. $\pi^+ p \rightarrow \rho^0 \Delta^{++}$. The $d\sigma/dt$ distribution is shown in Fig. 3. Disregarding the kinematically produced dip¹² at small $|t|$ ($\lesssim 0.05 \text{ GeV}^2$), the distribution exhibits a large forward peak with no turnover in the forward direction. A gradual change in curvature is observed into the large-momentum-transfer region, with a possible break in slope at $|t| \approx 0.7 \text{ GeV}^2$.

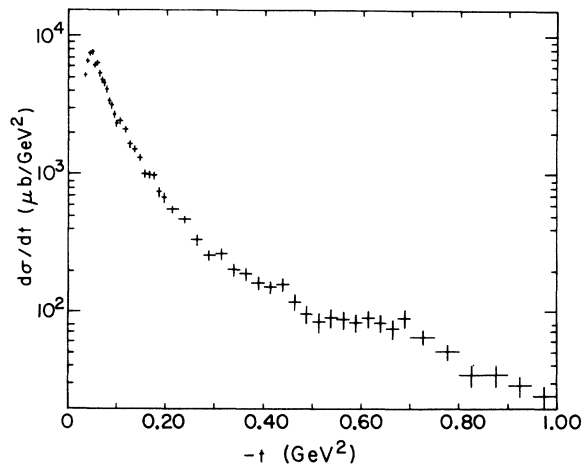


FIG. 3. Differential cross section, $d\sigma/dt$, for the reaction $\pi^+ p \rightarrow \rho^0 \Delta^{++}$ (1238), shown plotted as a function of momentum transfer.

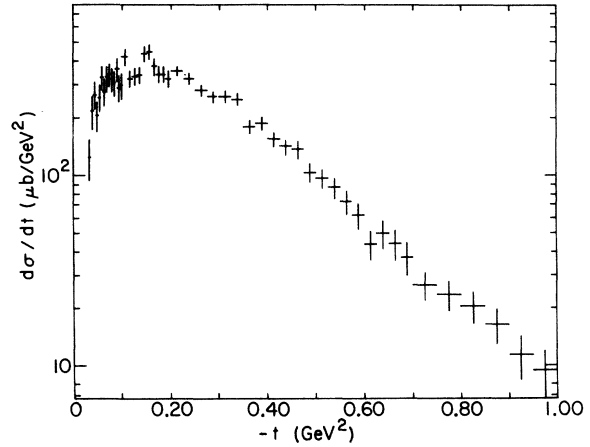


FIG. 4. Differential cross section, $d\sigma/dt$, for the reaction $\pi^+ p \rightarrow \omega \Delta^{++}$ (1238), shown plotted as a function of momentum transfer.

b. $\pi^+ p \rightarrow \omega \Delta^{++}$. The distribution shown in Fig. 4 is observed to be more or less flat for $|t| \leq 0.20 \text{ GeV}^2$, with some evidence for a dip in the very small $|t|$ region (disregarding the $|t| \approx 0.05 \text{ GeV}^2$ points; see above). For larger values of $|t|$ the distribution shows an exponential falloff with momentum transfer.

3. The $\rho_{mm'}$ distributions

a. $\pi^+ p \rightarrow \rho^0 \Delta^{++}$. The values of the $\rho_{mm'}^{J,H}$, are given in Table II and in Figs. 5(a)–5(f).¹³ The large statistics of the present experiment allow us to provide the density matrix elements in finer bins of momentum transfer than was possible previously: The $\rho_{mm'}$ distributions in the small $-t$ region ($|t| < 0.1 \text{ GeV}^2$) are given in great detail in Table IV.

We note the following features of the distributions:

(i) ρ_{00}^J , shown in Fig. 5(a), measures the unnatural-parity (UNP) contribution to the t -channel helicity-zero vector-meson states. We observe the dominance of UNP at small $|t|$ through its large (≈ 0.9) value. Note that, even at the smallest value of $|t|$ investigated, ρ_{00}^J is smaller than 1, which implies the need for contributions in addition to simple π exchange. Such corrections can come from, for example, absorptive corrections.^{14,15} For $|t|$ values beyond 0.2 GeV^2 ρ_{00}^J starts to decrease, and by $|t| \approx 0.6 \text{ GeV}^2$ it has a value consistent with zero.

(ii) ρ_{1-1}^J , shown in Fig. 5(b), is proportional to the difference between the natural- and unnatural-parity contributions to the t -channel helicity-one states. ρ_{1-1}^J is negative (UNP > NP) for $|t| \lesssim 0.35 \text{ GeV}^2$ and becomes positive in the large $-t$

TABLE I. $d\sigma/dt$ vs. t for reactions $\pi^+p \rightarrow \rho\Delta^{++}$ (1238), $\pi^+p \rightarrow \omega\Delta^{++}$ (1238).

$-t$ bin (GeV ²)	No. of events	ω $d\sigma/dt$ ($\mu\text{b}/\text{GeV}^2$)	No. of events	ρ $d\sigma/dt$ ($\mu\text{b}/\text{GeV}^2$)
0.030-0.035	20	124.4±31.1	749	5149.1±224.6
0.035-0.040	35	217.7±44.0	954	6558.4±263.6
0.040-0.045	53	265.5±45.4	1032	7517.0±270.2
0.045-0.050	41	205.4±38.3	1046	7618.9±272.5
0.050-0.055	54	257.5±42.2	919	6092.2±251.0
0.055-0.060	69	329.0±49.7	952	6311.0±257.1
0.060-0.065	58	275.8±45.3	873	5308.5±274.2
0.065-0.070	69	328.1±51.1	783	4761.3±252.0
0.070-0.075	65	339.6±50.5	755	4560.1±248.8
0.075-0.080	61	318.7±48.5	680	4107.1±229.5
0.080-0.085	53	304.4±46.9	598	3406.3±213.3
0.085-0.090	63	361.8±52.1	551	3138.6±200.1
0.090-0.095	56	287.5±46.4	509	2728.6±186.2
0.095-0.100	58	297.8±47.4	434	2326.5±164.5
0.100-0.110	139	418.3±40.3	792	2437.2±135.1
0.110-0.120	107	322.0±34.5	686	2111.0±120.7
0.120-0.130	114	330.9±35.3	583	1653.3±109.8
0.130-0.140	116	336.7±35.7	533	1511.5±102.2
0.140-0.150	138	435.8±40.5	492	1320.7±87.7
0.150-0.160	141	445.3±41.0	373	1001.3±71.2
0.160-0.170	121	375.0±38.7	348	996.8±74.1
0.170-0.180	109	337.8±36.4	341	976.8±72.9
0.180-0.190	118	338.8±35.0	282	746.6±67.5
0.190-0.200	112	321.6±33.9	257	680.4±62.8
0.200-0.225	274	352.9±23.2	512	559.8±38.4
0.225-0.250	249	320.7±21.9	434	474.5±33.7
0.250-0.275	226	279.2±19.8	329	333.9±29.2
0.275-0.300	209	258.2±19.0	255	258.8±23.9
0.300-0.325	200	258.5±19.8	246	263.7±26.2
0.325-0.350	193	249.4±19.4	190	203.7±21.5
0.350-0.375	141	179.9±16.6	166	189.7±21.4
0.375-0.400	147	187.5±17.0	143	163.4±19.1
0.400-0.425	126	155.2±15.0	135	152.5±16.9
0.425-0.450	115	141.6±14.3	140	158.1±17.3
0.450-0.475	116	136.6±14.8	118	118.2±17.4
0.475-0.500	88	103.6±12.5	96	96.2±14.7
0.500-0.525	77	96.3±12.0	80	83.9±14.2
0.525-0.550	69	86.3±11.3	86	90.2±15.0
0.550-0.575	66	73.0±11.0	75	87.4±13.9
0.575-0.600	56	61.9±9.8	71	82.7±13.4
0.600-0.625	36	43.5±8.0	74	89.0±13.2
0.625-0.650	41	49.6±8.7	68	81.8±12.4
0.650-0.675	34	43.9±8.2	65	74.6±12.8
0.675-0.700	29	37.5±7.5	78	89.5±14.7
0.700-0.750	54	26.5±4.6	105	65.0±8.0
0.750-0.800	48	23.6±4.2	82	50.7±6.8
0.800-0.850	40	20.5±4.0	58	34.2±6.2
0.850-0.900	32	16.4±3.4	58	34.2±6.2
0.900-0.950	23	11.4±3.0	48	28.7±4.9
0.950-1.000	19	9.5±2.7	41	24.0±4.5

TABLE II. Density-matrix elements vs. t for reaction $\pi^+p \rightarrow \rho\Delta^{++}$ (1238).

$-t$ bin (GeV ²)	No. of events	Fraction	Jackson frame		Helicity frame			
			ρ_{00}	ρ_{1-1}	ρ_{00}	ρ_{1-1}		
0.030-0.040	1703	0.840±0.020	0.910±0.020	-0.010±0.012	-0.030±0.015	0.880±0.020	-0.021±0.013	0.097±0.015
0.040-0.050	2078	0.880±0.015	0.900±0.020	-0.021±0.015	-0.048±0.015	0.870±0.022	-0.040±0.015	0.110±0.015
0.050-0.060	1871	0.810±0.020	0.910±0.021	-0.020±0.015	-0.075±0.016	0.860±0.020	-0.036±0.014	0.140±0.016
0.060-0.070	1656	0.744±0.030	0.922±0.027	0.003±0.017	-0.088±0.018	0.842±0.028	-0.032±0.018	0.195±0.017
0.070-0.080	1435	0.738±0.030	0.932±0.027	-0.015±0.018	-0.077±0.019	0.805±0.027	-0.072±0.018	0.229±0.018
0.080-0.090	1149	0.701±0.029	0.914±0.028	-0.019±0.018	-0.107±0.020	0.799±0.030	-0.080±0.019	0.235±0.020
0.090-0.100	943	0.654±0.030	0.872±0.030	-0.033±0.020	-0.147±0.019	0.808±0.030	-0.065±0.020	0.210±0.020
0.100-0.120	1478	0.758±0.031	0.847±0.029	-0.050±0.016	-0.124±0.017	0.715±0.028	-0.115±0.019	0.225±0.019
0.120-0.140	1116	0.694±0.028	0.874±0.027	-0.034±0.018	-0.135±0.018	0.685±0.030	-0.128±0.021	0.267±0.021
0.140-0.160	865	0.673±0.036	0.841±0.035	-0.049±0.021	-0.150±0.022	0.672±0.032	-0.143±0.015	0.270±0.020
0.160-0.180	689	0.693±0.037	0.814±0.024	-0.092±0.025	-0.167±0.025	0.662±0.033	-0.168±0.015	0.260±0.023
0.180-0.200	539	0.645±0.046	0.802±0.043	-0.048±0.029	-0.164±0.029	0.573±0.045	-0.164±0.012	0.271±0.027
0.200-0.250	946	0.674±0.035	0.759±0.035	-0.055±0.022	-0.152±0.021	0.506±0.032	-0.181±0.025	0.260±0.023
0.250-0.300	584	0.628±0.044	0.766±0.047	-0.055±0.031	-0.129±0.029	0.405±0.041	-0.238±0.034	0.241±0.027
0.300-0.350	436	0.661±0.050	0.599±0.048	0.073±0.037	-0.106±0.030	0.266±0.045	-0.097±0.043	0.194±0.030
0.350-0.400	309	0.702±0.055	0.509±0.059	-0.005±0.049	-0.128±0.034	0.380±0.059	-0.068±0.050	0.147±0.033
0.400-0.450	275	0.689±0.062	0.267±0.065	0.114±0.057	-0.022±0.035	0.274±0.058	0.118±0.046	0.032±0.035
0.450-0.500	214	0.610±0.072	0.274±0.079	0.148±0.067	0.016±0.047	0.241±0.074	0.131±0.071	0.001±0.044
0.500-0.550	166	0.642±0.082	0.318±0.085	0.200±0.077	-0.005±0.047	0.176±0.084	0.125±0.075	0.004±0.049
0.550-0.600	146	0.711±0.074	0.222±0.076	0.155±0.072	0.079±0.046	0.263±0.081	0.171±0.072	-0.066±0.044
0.600-0.650	142	0.733±0.081	0.074±0.061	0.292±0.076	0.024±0.042	0.191±0.066	0.349±0.045	-0.025±0.031
0.650-0.700	143	0.693±0.073	0.043±0.065	0.265±0.062	0.067±0.024	0.260±0.081	0.358±0.066	-0.036±0.040
0.700-0.800	187	0.744±0.070	0.001±0.060	0.218±0.070	0.008±0.032	0.300±0.059	0.341±0.041	0.034±0.045
0.800-0.900	116	0.721±0.083	0.084±0.055	0.216±0.077	0.008±0.039	0.252±0.094	0.302±0.085	0.025±0.054
0.900-1.000	89	0.715±0.090	0.000±0.070	0.253±0.090	-0.006±0.050	0.233±0.058	0.324±0.090	0.082±0.060

TABLE III. Density-matrix elements vs t for reaction $\pi^+p \rightarrow \omega\Delta^{++}(1238)$.

$-t$ bin (GeV ²)	No. of events	Fraction	Jackson frame			Helicity frame		
			ρ_{00}	ρ_{1-1}	$\text{Re}(\rho_{10})$	ρ_{00}	ρ_{1-1}	$\text{Re}(\rho_{10})$
0.030-0.040	55	0.900±0.100	0.636±0.101	-0.040±0.086	-0.099±0.059	0.669±0.099	-0.014±0.082	-0.023±0.063
0.040-0.050	94	0.725±0.074	0.324±0.100	0.133±0.084	0.027±0.056	0.290±0.097	0.116±0.086	0.050±0.056
0.050-0.060	123	0.691±0.071	0.564±0.095	-0.002±0.069	-0.159±0.053	0.647±0.008	0.037±0.080	-0.022±0.057
0.060-0.070	127	0.688±0.068	0.464±0.086	-0.102±0.071	-0.038±0.059	0.483±0.088	-0.093±0.069	0.006±0.058
0.070-0.080	126	0.757±0.065	0.341±0.082	0.173±0.064	-0.059±0.043	0.373±0.078	0.189±0.065	0.037±0.043
0.080-0.090	116	0.831±0.057	0.413±0.076	0.162±0.059	-0.103±0.044	0.459±0.084	0.188±0.065	0.055±0.044
0.090-0.100	114	0.742±0.068	0.225±0.088	0.201±0.059	-0.099±0.042	0.354±0.071	0.264±0.030	-0.020±0.052
0.100-0.120	246	0.870±0.040	0.443±0.053	0.154±0.042	-0.057±0.030	0.396±0.053	0.128±0.043	0.094±0.030
0.120-0.140	230	0.840±0.044	0.422±0.057	0.142±0.045	-0.077±0.032	0.395±0.055	0.128±0.046	0.096±0.032
0.140-0.160	279	0.915±0.034	0.285±0.046	0.146±0.042	-0.103±0.027	0.385±0.049	0.195±0.041	0.039±0.027
0.160-0.180	230	0.904±0.041	0.363±0.062	0.094±0.045	-0.081±0.031	0.383±0.051	0.102±0.040	0.069±0.028
0.180-0.200	230	0.831±0.041	0.382±0.056	0.242±0.048	-0.105±0.030	0.310±0.055	0.207±0.050	0.137±0.028
0.200-0.250	523	0.931±0.024	0.277±0.033	0.160±0.028	-0.056±0.019	0.288±0.032	0.166±0.028	0.053±0.019
0.250-0.300	435	0.894±0.026	0.281±0.038	0.120±0.032	-0.090±0.020	0.342±0.035	0.151±0.030	0.071±0.020
0.300-0.350	393	0.936±0.027	0.250±0.037	0.178±0.034	-0.112±0.020	0.301±0.039	0.205±0.032	0.101±0.020
0.350-0.400	288	0.923±0.024	0.241±0.039	0.155±0.041	-0.088±0.024	0.285±0.046	0.177±0.039	0.076±0.025
0.400-0.450	241	0.892±0.039	0.292±0.051	0.214±0.042	-0.082±0.028	0.190±0.043	0.163±0.029	0.100±0.025
0.450-0.500	204	0.850±0.047	0.303±0.058	0.107±0.054	-0.118±0.033	0.285±0.060	0.098±0.051	0.119±0.033
0.500-0.550	146	0.906±0.046	0.465±0.070	-0.006±0.057	-0.188±0.037	0.311±0.064	-0.086±0.065	0.192±0.036
0.550-0.600	122	0.795±0.072	0.351±0.077	-0.074±0.067	-0.169±0.049	0.414±0.077	-0.043±0.064	0.169±0.048
0.600-0.650	77	0.875±0.070	0.450±0.087	-0.013±0.068	-0.194±0.049	0.278±0.081	-0.100±0.085	0.194±0.055
0.650-0.700	63	0.931±0.070	0.427±0.104	0.032±0.082	-0.145±0.054	0.226±0.095	-0.066±0.086	0.133±0.060
0.700-0.800	102	0.704±0.079	0.550±0.095	0.030±0.065	-0.230±0.051	0.111±0.100	-0.180±0.090	0.184±0.060
0.800-0.900	72	0.742±0.086	0.546±0.109	0.033±0.095	-0.157±0.076	0.131±0.113	-0.175±0.093	0.094±0.064
0.900-1.000	42	0.724±0.091	0.522±0.132	0.045±0.106	-0.202±0.055	0.086±0.124	-0.175±0.142	0.114±0.071

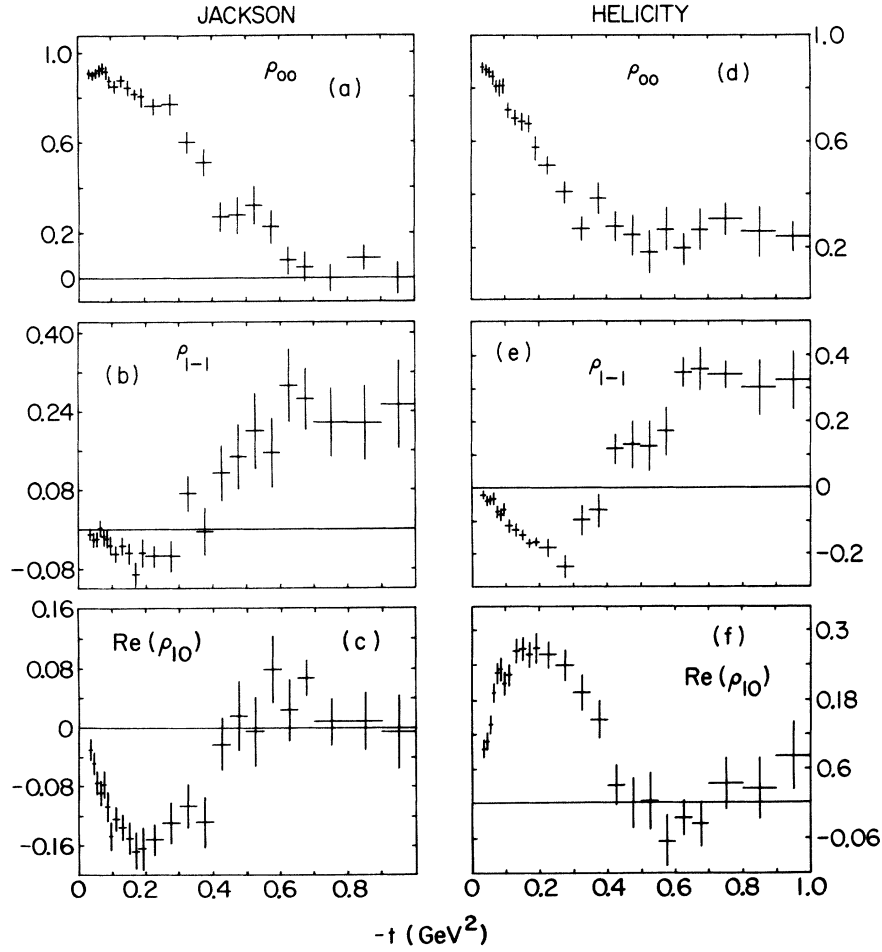


FIG. 5. (a)–(c) The values of the ρ^0 density-matrix elements from the reaction $\pi^+p \rightarrow \rho^0\Delta^{++}(1238)$ as evaluated in the Jackson frame. (d)–(f) Same as (a)–(c), but the ρ_{mn}^H are evaluated in the helicity frame.

region, where natural-parity (NP) exchange becomes important.

(iii) $\text{Re}\rho_{10}^J$, shown in Fig. 5(c), is negative at low $|t|$, as observed in many other reactions involving vector-meson production. The distribution reaches a minimum at $|t| \approx 0.2 \text{ GeV}^2$ and then rises to become zero for $|t| \gtrsim 0.45 \text{ GeV}^2$.

(iv) ρ_{00}^H , shown in Fig. 5(d), measures the UNP contribution to helicity-zero s -channel production. The ρ_{00}^H distribution is observed to be large at small $|t|$, and to fall more rapidly than does the corresponding ρ_{00}^J distribution. For $|t|$ values between 0.3 and 1.0 GeV^2 , ρ_{00}^H is essentially constant at a value of ≈ 0.25 . Note that this is in contrast to ρ_{00}^J , which appears to fall to zero for $|t| > 0.6 \text{ GeV}^2$.

(v) ρ_{1-1}^H , shown in Fig. 5(e), is proportional to the difference between the NP and UNP contributions to the s -channel helicity-one states. Like ρ_{1-1}^J , ρ_{1-1}^H is observed to be negative for $|t| \leq 0.4$

GeV^2 and positive in the large $-t$ region. However, ρ_{1-1}^H appears to decrease more rapidly at small $|t|$ than does ρ_{1-1}^J . A minimum at $|t| \approx 0.25 \text{ GeV}^2$ is observed whose absolute value is larger by a factor of 2 than that of ρ_{1-1}^J and signals a proportionally larger amount of helicity-one UNP in the s channel.

(vi) $\text{Re}\rho_{10}^H$, shown in Fig. 5(f), is observed to rise more rapidly than $\text{Re}\rho_{10}^J$ decreases in the small $|t|$ region. This same behavior is also observed, for example, in the reaction $K^+p \rightarrow K^{*0}(890)\Delta^{++}(1238)$.¹⁴

We proceed to examine linear combinations of the above ρ_{mn} , which serve to project out NP and UNP helicity-one contributions.

(vii) $\rho_+ = \rho_{11} + \rho_{1-1}$ (frame invariant) projects out the total NP contribution to the helicity-one states and is shown in Fig. 6(a). A small, but significant, value is observed for $|t| < 0.2 \text{ GeV}^2$. Beyond this value of $|t|$ the NP contribution increases

TABLE IV. Density-matrix elements vs t for reaction $\pi^+p \rightarrow \rho\Delta^{++}$ (1238) (fine bins).

$-t$ bin (GeV ²)	No. of events	Jackson frame		Helicity frame	
		ρ_{00}	ρ_{1-1}	ρ_{00}	ρ_{1-1}
0.030-0.032	268	0.770±0.050	0.014±0.028	0.950±0.030	0.006±0.030
0.032-0.034	310	0.740±0.050	0.008±0.029	0.900±0.037	0.007±0.031
0.034-0.036	338	0.840±0.030	-0.018±0.019	0.900±0.033	-0.023±0.020
0.036-0.038	388	0.860±0.026	-0.020±0.024	0.960±0.024	-0.019±0.019
0.038-0.040	399	0.880±0.025	-0.020±0.021	0.860±0.030	-0.039±0.020
0.040-0.042	414	0.890±0.025	-0.030±0.020	0.870±0.030	-0.042±0.020
0.042-0.044	422	0.870±0.030	0.013±0.023	0.870±0.030	-0.010±0.024
0.044-0.046	395	0.880±0.026	-0.026±0.027	0.770±0.040	-0.050±0.026
0.046-0.048	432	0.890±0.024	-0.012±0.023	0.860±0.030	-0.018±0.023
0.048-0.050	415	0.900±0.023	0.028±0.021	0.800±0.037	-0.023±0.023
0.050-0.052	373	0.790±0.030	-0.019±0.020	0.900±0.032	-0.047±0.023
0.052-0.054	361	0.840±0.029	0.030±0.020	0.870±0.030	0.008±0.023
0.054-0.056	394	0.820±0.031	-0.023±0.028	0.840±0.035	-0.031±0.028
0.056-0.058	376	0.790±0.032	0.007±0.024	0.840±0.033	-0.018±0.022
0.058-0.060	367	0.740±0.032	0.004±0.025	0.850±0.037	-0.035±0.027
0.060-0.065	873	0.757±0.035	-0.002±0.019	0.836±0.031	-0.025±0.020
0.065-0.070	783	0.679±0.031	-0.028±0.020	0.856±0.031	-0.047±0.022
0.070-0.075	755	0.786±0.035	-0.008±0.020	0.761±0.032	-0.067±0.021
0.075-0.080	680	0.728±0.036	-0.036±0.021	0.781±0.032	-0.103±0.020
0.080-0.085	598	0.716±0.041	0.004±0.021	0.809±0.033	-0.070±0.023
0.085-0.090	551	0.655±0.043	-0.044±0.023	0.790±0.035	-0.104±0.025
0.090-0.095	509	0.654±0.045	-0.053±0.023	0.873±0.040	-0.063±0.028

rapidly so that by $|t| \approx 0.5 \text{ GeV}^2$ it exceeds the total UNP contribution (i.e., $\rho_{00} + \rho_{-}$).

(viii) $\rho_{-}^J = \rho_{11}^J - \rho_{1-1}^J$ is proportional to the helicity-one UNP contribution and is shown in Fig. 6(b). The small, but significant, component at small $|t|$ increases in value with increasing $|t|$ and for $|t| \geq 0.4 \text{ GeV}^2$ is relatively constant at a value $\approx 0.20-0.25$.

(ix) $\rho_{-}^H = \rho_{11}^H - \rho_{1-1}^H$ projects out the s -channel UNP helicity-one contributions and is shown in Fig. 6(c). ρ_{-}^H is observed to rise rapidly from a significantly nonzero value at low $|t|$ to a maximum of ~ 0.45 at $|t| \approx 0.3 \text{ GeV}^2$. Beyond this value of momentum transfer it decreases rapidly, and for $|t| > 0.6 \text{ GeV}^2$ it is quite small though significantly positive.

The behavior of the $\rho_{mm'}$, discussed above, leads to the conclusion that UNP exchange is the dominant contributor in the low-momentum-transfer region. However, even at the smallest $-t$ investigated ($\approx 0.03 \text{ GeV}^2$) there are still a significant NP and UNP contributions to helicity-one vector-meson production. Natural-parity exchange becomes significant in the high $|t|$ region where ρ_{00}^H and ρ_{1-1}^H become small, ρ_{00}^J is consistent with zero, and ρ_{-}^J has a value of ~ 0.2 .

b. $\pi^+ p \rightarrow \omega \Delta^{++}$. The values of $\rho_{mm'}$ are given in Table III. They have been previously determined, using a somewhat different technique, by Buhl *et al.*² Their results are similar to those presented here.

(i) ρ_{00}^J is shown in Fig. 7(a) and is quite large (~ 0.5) in the low-momentum-transfer region. A decrease in value results in a broad minimum in the region $0.2 \leq |t| \leq 0.5 \text{ GeV}^2$. At larger values of $|t|$ the helicity-zero UNP fraction is observed to increase in value. Note that, in contrast to the observation of Abrams *et al.*,¹⁶ who studied reaction (4) at $3.7 \text{ GeV}/c$, there is no indication for a sharp dip in ρ_{00}^J at or near $-t \approx 0.25 \text{ GeV}^2$.

(ii) ρ_{1-1}^J , shown in Fig. 7(b), is observed to rise from 0.0 to a value of ~ 0.15 at $|t| = 0.1 \text{ GeV}^2$ (at the same time ρ_{00}^J is falling; see above). It remains constant in value until $|t| \sim 0.5 \text{ GeV}^2$, at which point it decreases to near zero and remains so until $|t| \sim 1.0 \text{ GeV}^2$.

(iii) $\text{Re}\rho_{10}^J$ is shown in Fig. 7(c). As in the $\rho^0 \Delta^{++}$ reaction, $\text{Re}\rho_{10}^J$ is negative at small $|t|$. In contrast to that observed in $\rho \Delta$ there is no turnover toward zero, but rather a further decrease at larger $|t|$.

(iv) ρ_{00}^H is shown in Fig. 7(d) and has a value of ~ 0.4 at low $-t$. The distribution shows a gradual decrease in value into the large-momentum-transfer region.

(v) ρ_{1-1}^H , shown in Fig. 7(e), appears similar in shape to the corresponding ρ_{1-1}^J ; however, in

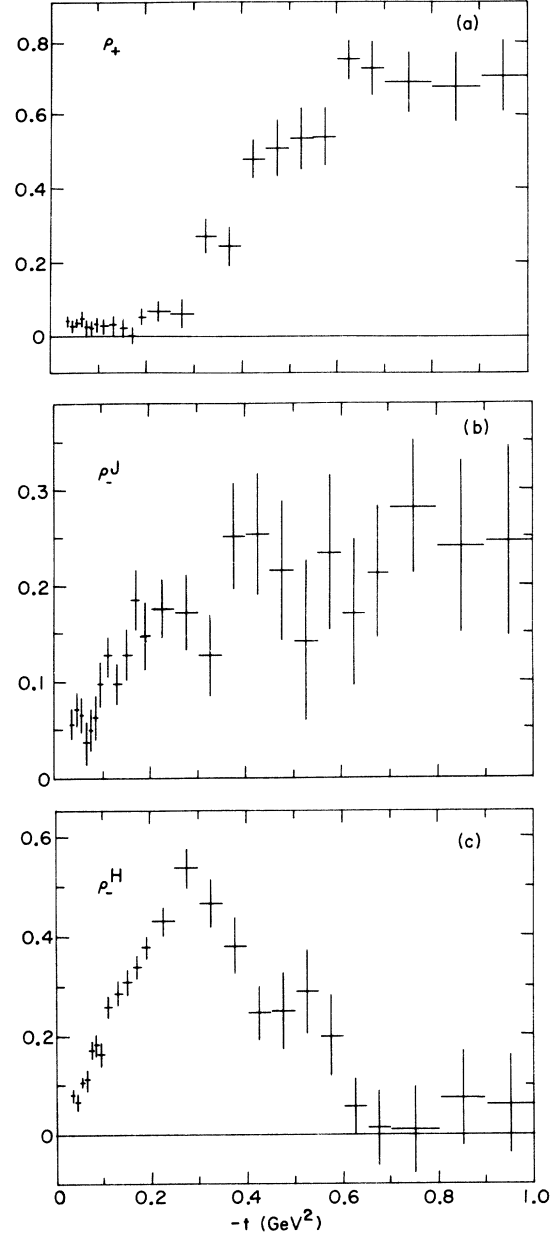


FIG. 6. (a) The natural-parity helicity-one projection, $(\rho_{11} + \rho_{1-1})$, shown as a function of momentum transfer for the reaction $\pi^+ p \rightarrow \rho^0 \Delta^{++}$ (1238). (b) The unnatural-parity helicity-one projection, $\rho_{11} - \rho_{1-1}$ (in the Jackson frame), for the reaction $\pi^+ p \rightarrow \rho^0 \Delta^{++}$. (c) Same as (b) but evaluated in the helicity frame.

the region $|t| > 0.5 \text{ GeV}^2$, ρ_{1-1}^H is observed to be significantly negative.

(vi) $\text{Re}\rho_{10}^H$ is shown in Fig. 7(f) and is observed to increase from zero at low $-t$ to ~ 0.10 at larger values of momentum transfer. As for $\text{Re}\rho_{10}^J$, the turnover at large $-t$ observed in $\rho \Delta$ (and $K^* \Delta$)¹⁴ is not observed here.

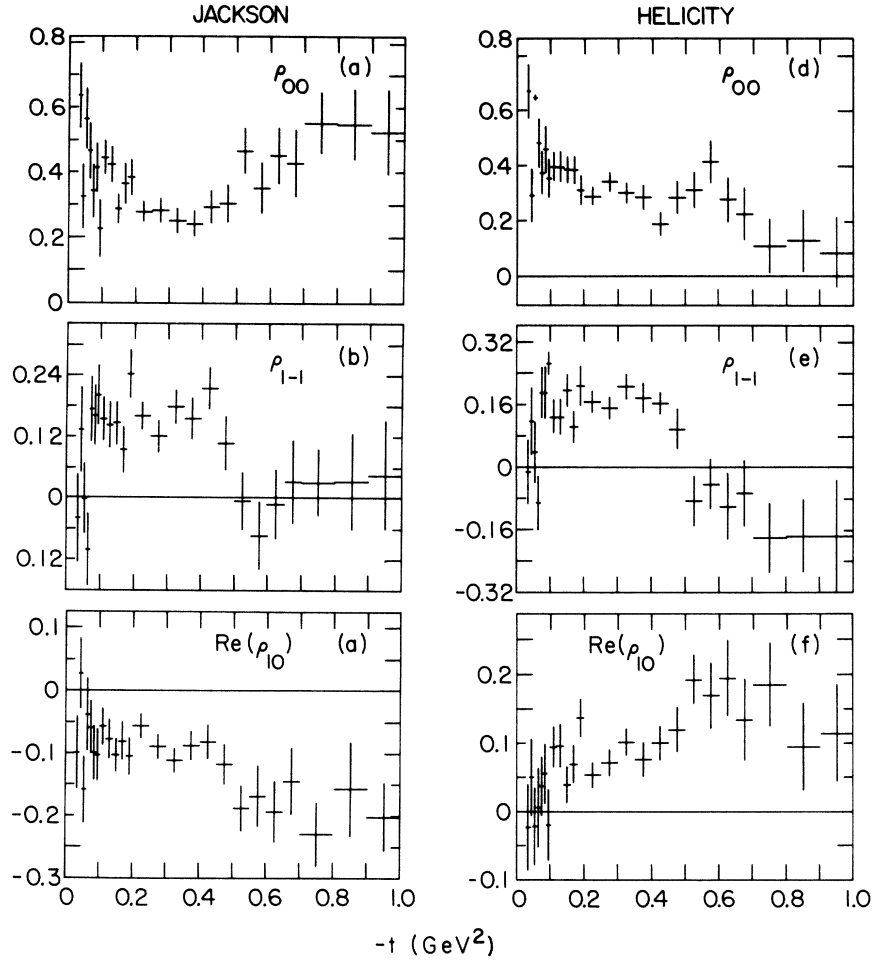


FIG. 7. (a)–(c) The values of the ω density-matrix elements from the reaction $\pi^+p \rightarrow \omega\Delta^{++}$ (1238) as evaluated in the Jackson frame. (d)–(f) Same as (a)–(c), but the $\rho_{mm'}$ are evaluated in the helicity frame.

(vii) ρ_+ [Fig. 8(a)], the natural-parity projection, rises from a value of ~ 0.15 at low $|t|$ to ~ 0.50 between 0.1 and 0.5 GeV^2 . It then decreases rapidly to a constant value of ~ 0.25 for $|t| > 0.5$ GeV^2 .

(viii) ρ_-^J [Fig. 8(b)] is rather featureless at a constant value of ~ 0.20 for all values of $|t|$.

(ix) ρ_-^H [Fig. 8(c)] shows a factor of ~ 6 increase between low and high values of momentum transfer.

Therefore, in reaction (4), there appear three momentum-transfer regions in which the relative NP and UNP contributions are different:

For $|t| \leq 0.10$ GeV^2 , $\rho_+ \sim 0.15$ with ρ_{00}^J dominating in the t -channel and ρ_{00}^H in the s -channel frame. UNP dominates.

For $0.1 \leq |t| \leq 0.4$ GeV^2 , ρ_+ is large (~ 0.50) and constant over the interval. ρ_{00}^J (ρ_-^J) is also constant at a value of ~ 0.3 (0.2). Likewise, ρ_{00}^H (ρ_-^H) is constant with a similar value. Here, then,

UNP \approx NP.

For $|t| > 0.4$ GeV^2 , ρ_+ decreases dramatically to an approximately constant value of 0.25 over this interval. ρ_{00}^J increases in value while ρ_-^J remains fairly constant; ρ_{00}^H decreases slightly with ρ_-^H showing a sizeable increase. Hence, in this region, UNP dominates.

IV. COMPARISON OF PRODUCTION PROPERTIES

A. $\rho_{00} d\sigma/dt$

The distribution $\rho_{00}^J d\sigma/dt$ ($\rho_{00}^H d\sigma/dt$), which directly measures the strength of the UNP contribution to t - (s -) channel helicity-zero states, is shown in Fig. 9 (10) for $\rho^0\Delta^{++}$. In both frames, $\rho_{00} d\sigma/dt$ is observed to have a strong forward peak which is as expected from the dominant π -exchange contribution to the nonflip ($n=0$) s - and t -channel amplitudes. Note the change in slope of $\rho_{00}^H d\sigma/dt$ at $|t| \sim 0.4$ GeV^2 . A similar structure

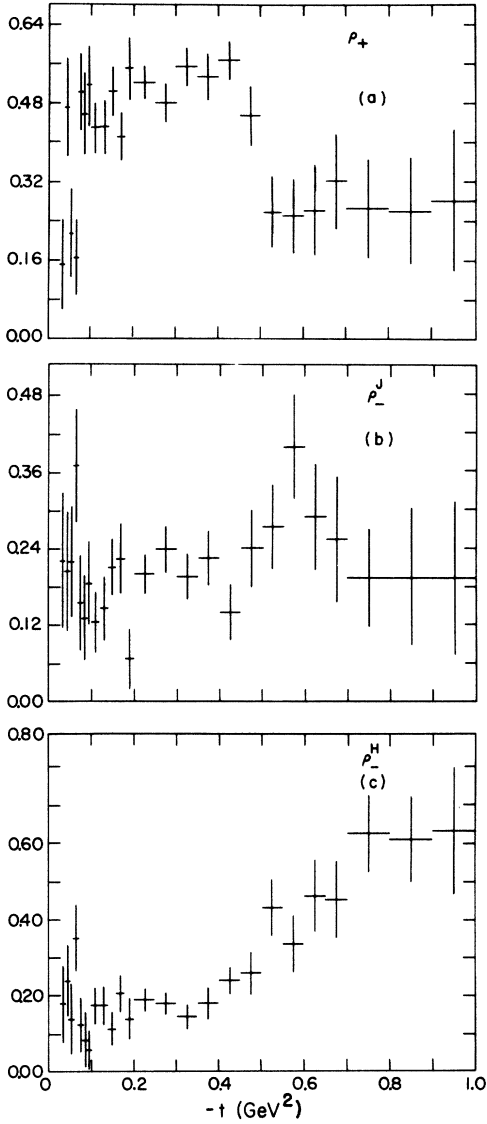


FIG. 8. (a) The natural-parity helicity-one projection, $\rho_{11} + \rho_{1-1}$, shown as a function of momentum transfer for the reaction $\pi^+p \rightarrow \omega\Delta^{++}$. (b) The unnatural-parity helicity-one projection, $\rho_{11} - \rho_{1-1}$, in the Jackson frame, for the reaction $\pi^+p \rightarrow \omega\Delta^{++}$ (1238). (c) Same as (b) but evaluated in the helicity frame.

has been observed in the reaction $\pi^-p \rightarrow \rho^0n$ at 6.0 and 17.2 GeV/c. However, the amplitude structure of $\rho_{00}^H d\sigma/dt$ in ρ^0n and $\rho^0\Delta^{++}$ is quite different, so that arguments¹⁷ which conclude that the break in slope (in ρ^0n) cannot be fitted within the framework of π exchange plus only $n=0$ cuts may not be applicable to the Δ^{++} associated reaction.

Expecting the π propagator, even in the presence of absorptive corrections, to dominate the helicity-zero amplitudes, we have fitted $\rho_{00} d\sigma/dt$ to the

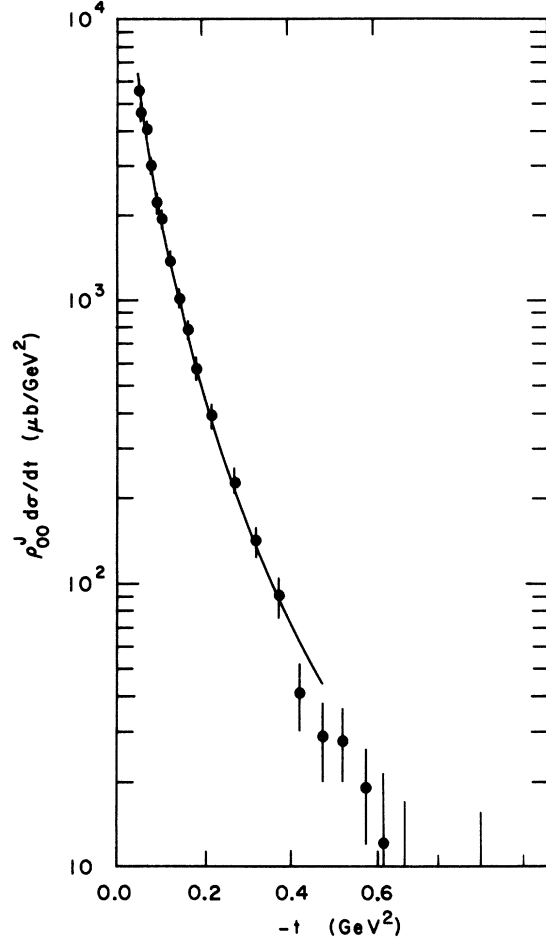


FIG. 9. The $\rho_{00}^J d\sigma/dt$ (UNP t -channel helicity-zero) distribution shown as a function of momentum transfer for the reaction $\pi^+p \rightarrow \rho^0\Delta^{++}$ (1238). The solid curve represents the results of a fit to the form $A e^{b|t|} / (t - \mu^2)^2$.

simple form

$$\rho_{00} \frac{d\sigma}{dt} = \frac{A e^{b|t|}}{(t - \mu^2)^2},$$

where $\mu^2 = m_\pi^2$. The results of the fit for $|t| < 0.5$ GeV² are shown as the solid curve in Fig. 9 (10), with

$$\rho_{00}^H \frac{d\sigma}{dt}, \quad A = (40.5 \pm 1.4) \mu\text{b GeV}^2,$$

$$b = -4.2 \pm 0.3 \text{ GeV}^{-2},$$

$$\rho_{00}^J \frac{d\sigma}{dt}, \quad A = (40.8 \pm 1.2) \mu\text{b GeV}^2,$$

$$b = -2.7 \pm 0.2 \text{ GeV}^{-2}.$$

The results indicate that neither of the distributions can be represented solely by the π propagator; an additional exponential damping factor is needed to fit the distribution away from the near

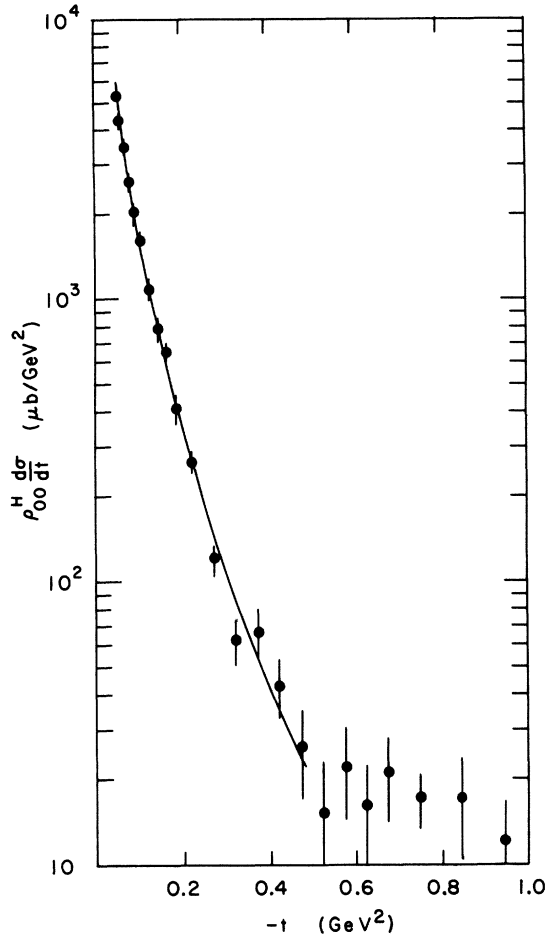


FIG. 10. The $\rho_{00}^H d\sigma/dt$ (UNP s -channel helicity-zero) distribution shown as a function of momentum transfer for the reaction $\pi^+p \rightarrow \rho^0\Delta^{++}$ (1238). The solid curve represents the results of a fit to the form $A e^{b|t|}/(t-\mu^2)^2$.

forward direction. It is important to note that, in the analysis of the corresponding distributions for the reaction¹⁴

$$K^+p \rightarrow K^{*0}(890)\Delta^{++}$$

from 4.6 to 16.0 GeV/c, for all energies, the value of b in the t -channel (s -channel) frame was consistent with zero (~ 1.0 GeV⁻²) with no shrinkage indicated. It can be seen from the larger, significant value of $|b|$ in the $\pi^+p \rightarrow \rho^0\Delta^{++}$ reaction (where only π exchange can contribute) that the small value and energy-independent behavior of b in $K^+p \rightarrow K^{*0}(890)\Delta^{++}$ (where π and B exchange contribute) cannot be used to argue either for a nonshrinking pion or for a universal fit to $1/(t-\mu^2)^2$ to all¹⁸ UNP helicity-zero cross sections. What we do learn is that $\rho_{00} d\sigma/dt$ for $\rho\Delta$ and $K^{*0}\Delta$ have dominant contributions from π exchange as exhibited by the excellent fits to

forms which include the π propagator.

In contrast to $\rho_{00}^J d\sigma/dt$ ($\rho^0\Delta^{++}$) the corresponding distributions for $\pi^+p \rightarrow \omega\Delta^{++}$ [see Figs. 11(a) and 11(b)] which cannot have a π -exchange contribution, show no strong forward peaks and are rather flat for $|t| < 0.2$ GeV². Of interest is the relative ρ/ω ratio of the respective $\rho_{00} d\sigma/dt$ distributions. If the only contribution to $\rho_{00} d\sigma/dt$ is from exchange-degenerate π and B Regge poles, then it can easily be shown that¹⁸

$$\frac{\rho_{00} \frac{d\sigma}{dt}(\rho^0\Delta^{++})}{\rho_{00} \frac{d\sigma}{dt}(\omega\Delta^{++})} = A \cot^2\left(\frac{\pi\alpha(t)}{2}\right), \quad (8)$$

with $\alpha(t) = \alpha'(0)(t - m_\pi^2)$ and where A is a constant independent of momentum transfer. The requirement that the sum of the π plus B pole terms in $K^+p \rightarrow K^{*0}\Delta^{++}$ be real leads to the expectation of π - B strong exchange degeneracy. This and SU(3) at the meson vertex produce the prediction $A = 1$.¹⁹ The ρ/ω ratio in the Jackson (helicity) frame is shown in Fig. 12 (13). In each case, the solid curve represents the result of the fit to the exchange-degenerate (EXD) from (8) which, especial-

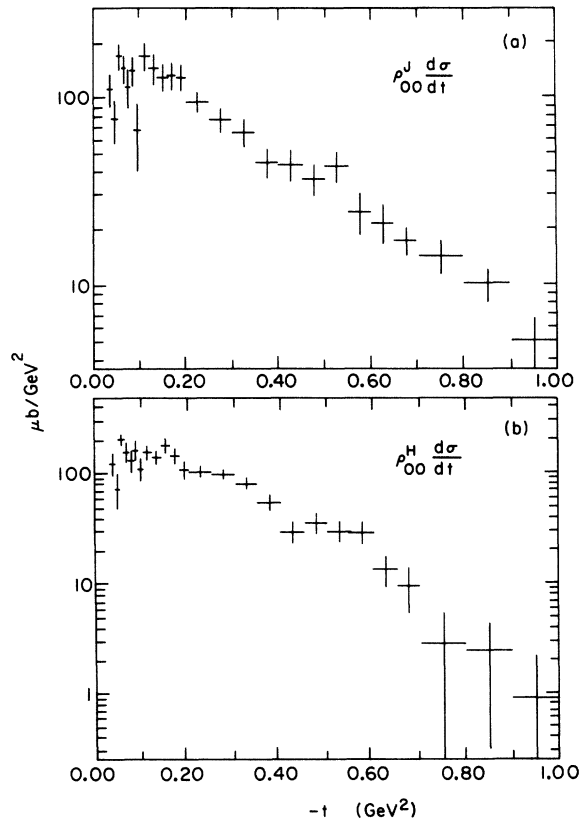


FIG. 11. (a) $\rho_{00}^J d\sigma/dt$ for $\pi^+p \rightarrow \omega\Delta^{++}$. (b) $\rho_{00}^H d\sigma/dt$ for $\pi^+p \rightarrow \omega\Delta^{++}$.

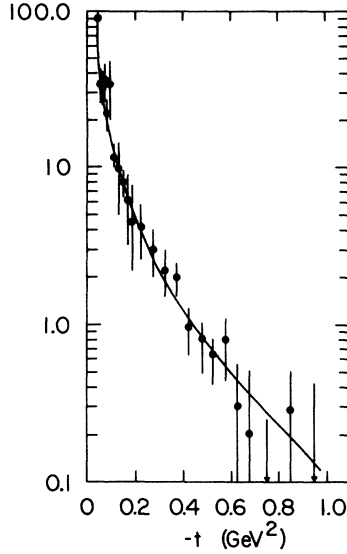


FIG. 12. The ρ/ω ratio of their respective $\rho_{00}^J d\sigma/dt$ distributions shown as a function of momentum transfer. The curve represents the results of a fit of this distribution to a form suggested by strong π - B exchange degeneracy.

ly in the Jackson frame, is an excellent parametrization of the data for all $|t|$. In the H frame there is some deviation from form (8) at large $|t|$. The results of the fit are

$$\rho_{00}^J \frac{d\sigma}{dt}: A=0.19 \pm 0.01, \quad \alpha'(0)=0.57 \pm 0.005,$$

$$P_{\chi^2}=0.93,$$

$$\rho_{00}^H \frac{d\sigma}{dt}: A=0.19 \pm 0.01, \quad \alpha'(0)=0.69 \pm 0.02,$$

$$P_{\chi^2}=0.04,$$

in disagreement with the SU(3) and strong-EXD prediction of $A=1$. The data are, however, consistent with a picture of weak exchange-degenerate π - B Regge poles in which the square of the ratio of the π and B residues equals 0.19. The data cannot rule out, in the framework of this simple description, some over-all small differences in the t dependence of the different exchange couplings.²⁰⁻²²

The values of A and $\alpha'(0)$ for $\rho_{00}^J d\sigma/dt$, in particular, are in disagreement with a similar determination¹⁶ at 3.7 GeV/ c in which $A=0.41$ and $\alpha'(0)=1.12$ were obtained, which leads to a wrong-signature nonsense zero in the π amplitude, and prediction of a dip in $\rho_{00}^J d\sigma/dt$ at $-t \sim 0.75$ GeV² for $\rho^0 \Delta^{++}$. The data of the present experiment show no significant evidence for a dip-rise structure in this distribution near this $|t|$ value. In addition, the difference between the values of A

and $\alpha'(0)$ at 3.7 GeV/ c and the present experiment, in light of the excellent fits with form (8) to the respective distributions [Figs. 12 and 13 of this paper and Fig. 4(a) of Ref. 13], results from the relatively much smaller ρ/ω cross-section ratio in the lower-energy data. It is possible that we are observing a strong energy dependence of this ratio, which would suggest that form (8) is no more than a useful parametrization of the data with very little physical substance. Alternatively, the discrepancy in the two experiments may be caused by the method of extraction of the relative cross sections. Even if the latter were true, one would expect more than just π and B pole exchange contributions to $\rho_{00} d\sigma/dt$ (e.g., π and B cut) which might be expected to destroy relationships derived from simple strong-exchange-degeneracy arguments for the pole terms.

B. $\rho_+ d\sigma/dt$

In Fig. 14(a) is shown the natural-parity exchange projection, $\rho_+ d\sigma/dt$, for the $\rho^0 \Delta^{++}$ reaction. Invoking current theoretical ideas^{15,17,23} on the phenomenology of vector-meson production we first observe that the NP pole A_2 contribution should be small at small $-t$, so that the large value of $\rho_+ d\sigma/dt$ for $|t| < 0.10$ GeV² is most naturally associated with π and A_2 cut contributions. At large values of momentum transfer ($|t| > 0.20$), the A_2 pole contribution dominates. The dip at $|t| \sim 0.15$ GeV² is interpreted, as in a similar structure in $\rho_+ d\sigma/dt$ in $\pi^- p \rightarrow \rho^0 n$,²³ as arising from interference between the A_2 pole and π and A_2 cut terms.

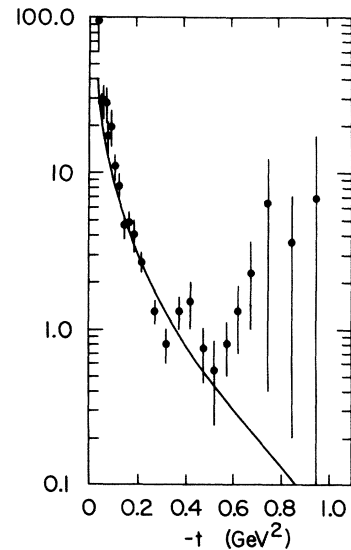


FIG. 13. Same as Fig. 12, but here the ρ/ω ratio of the $\rho_{00}^H d\sigma/dt$ distribution is shown.

In Fig. 15(a), the corresponding distribution for the $\omega\Delta^{++}$ reaction is exhibited, and should receive contributions from B cut plus ρ plus ρ cut. Note the lack of a dip in the distribution at $|t| \approx 0.6$ GeV^2 . If we were observing purely ρ pole, then expectations are for a dip in $\rho_+ d\sigma/dt$ corresponding to the wrong-signature nonsense zero of the ρ . The lack of dip structure at or near this t value is explained by $(\rho + B)$ -cut contributions filling in the dip from the simple ρ -pole exchange.

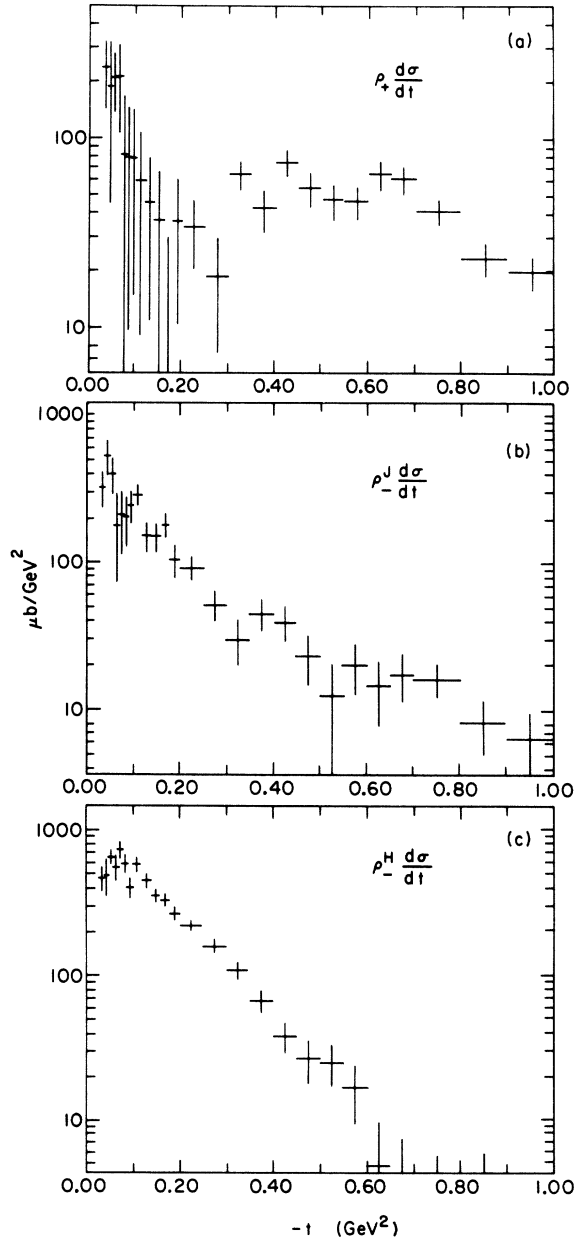


FIG. 14. (a) $\rho_+ d\sigma/dt[\pi^+p \rightarrow \rho^0\Delta^{++}(1238)]$, shown as a function of momentum transfer. (b) [(c)] Corresponding ρ_+^J [ρ_+^H] $d\sigma/dt$ distribution.

C. $\rho^{J,H} d\sigma/dt$

$\rho_-^J d\sigma/dt$ ($\rho_-^H d\sigma/dt$) is shown in Fig. 14(b) [Fig. 14(c)] for $\pi^+p \rightarrow \rho^0\Delta^{++}$ and in Fig. 15(b) [Fig. 15(c)] for the $\pi^+p \rightarrow \omega\Delta^{++}$ reaction, and is observed to be rather structureless. In the helicity frame this unnatural-parity exchange component receives contributions from UNP poles plus cuts and from NP cuts, and any simple description is masked by the problems of interferences among the different contributions.

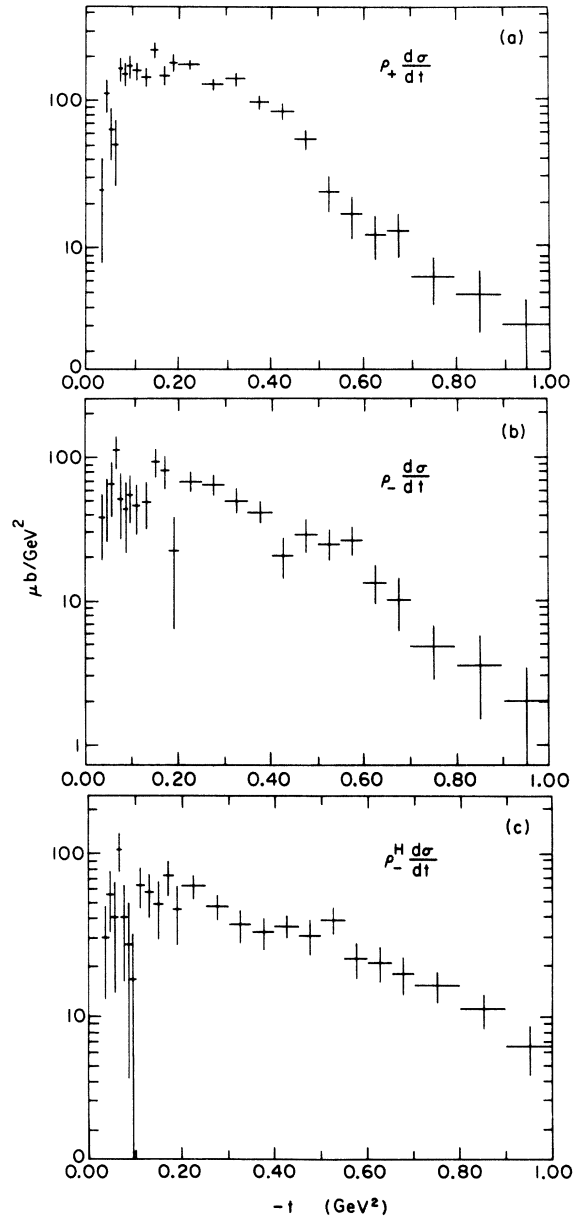


FIG. 15. (a) $\rho_+ d\sigma/dt[\pi^+p \rightarrow \omega\Delta^{++}(1238)]$, shown as a function of momentum transfer. (b) [(c)] Corresponding ρ_-^J [ρ_-^H] $d\sigma/dt$ distribution.

$\rho^J d\sigma/dt$ should receive no contribution from the (π, B) or (A_2, ρ) pole terms and is expected, therefore, to have contributions from only the respective cut terms. However, Michael²⁴ has pointed out the possibility that there is a nonzero π -exchange coupling to t channel helicity-one states so that π pole could contribute to $\rho^J d\sigma/dt$.

V. RESONANT STRUCTURE IN THE π^+p MASS SPECTRA NEAR 1.9 GEV

A. Properties of the Δ^{++} (1880)

We now turn to a discussion of our investigation of reactions (1), (2), and (5) for π^+p enhancements²⁵ with masses greater than that of the Δ^{++} (1238). To conduct this investigation we explored the π^+p mass spectra for events in the corresponding ρ , ω , and K^{*0} (890) mass bands. In addition, $\cos\theta^H$ [where θ^H is the (helicity) angle between the direction of the $p\pi^+$ system in the over-all center of mass and the outgoing π^+ in the $p\pi^+$ rest frame] was required to be greater than zero. Thus cut, which essentially selects events in one half of the $(\rho, \omega, K^*) \pi^+ - \pi^+p$ Dalitz plot, was required in order to look at the π^+p mass spectrum without having to contend with the large reflections of the $A_1(\rho\pi)$, $B(\omega\pi)$,²⁶ and $Q(K^*\pi)$ low-mass enhancements. The resultant $M(\pi^+p)$ mass spectra are shown in Fig. 16(a)–16(c), in which large, statistically significant signals are observed. The peaks in the mass spectra are all observed to lie somewhat lower than 1.90 GeV. The mass and width of the state were obtained from fits to the respective mass spectra in the interval 1.6–2.2 GeV. A form consisting of a linear background in mass and an S-wave Breit-Wigner shape multiplying phase space gave²⁷

$$\pi^+p \rightarrow \rho^0(\pi^+p): M = (1882 \pm 7) \text{ MeV},$$

$$\Gamma = (172 \pm 31) \text{ MeV};$$

$$\pi^+p \rightarrow \omega(\pi^+p): M = (1879 \pm 11) \text{ MeV},$$

$$\Gamma = (235 \pm 61) \text{ MeV};$$

$$K^+p \rightarrow K^{*0}(\pi^+p) \text{ (Ref. 28): } M = (1881 \pm 15) \text{ MeV},$$

$$\Gamma = (294 \pm 41) \text{ MeV}.$$

The values of mass and width are all consistent with each other and give a weighted average value for this Δ^{++} state of

$$M = (1881.2 \pm 5.5) \text{ MeV},$$

$$\Gamma = (219 \pm 23) \text{ MeV}.$$

We used an s-wave (rather than f-wave) Breit-Wigner form because at this high mass it is probably just as good a parametrization. Our quoted errors for Γ and M are statistical only and do not

take into account possible shifts due to changes in parametrization.

The πp phase-shift analyses⁹ have established three different $I = \frac{3}{2}$ states in this mass region, viz.,

$$\Delta(1890): J^P = \frac{5}{2}^+;$$

~17% branching ratio into $N\pi$,

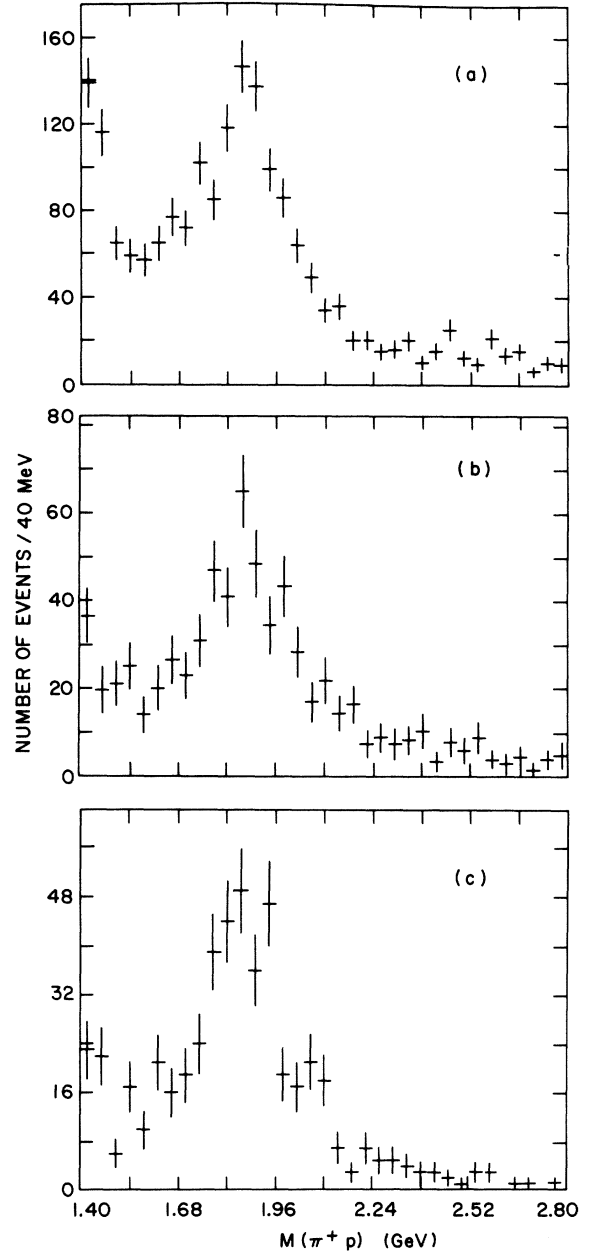


FIG. 16. (a) $p\pi^+$ effective-mass spectrum for events in the ρ region from the $\pi^+p \rightarrow \pi^+\pi^-\pi^+p$ final state ($\cos\theta^H > 0$). (b) $p\pi^+$ effective-mass spectrum for events in the ω region from the $\pi^+p \rightarrow \pi^+\pi^-\pi^0\pi^+p$ final state ($\cos\theta^H > 0$). (c) $p\pi^+$ effective-mass spectrum for events in the K^* region from the $K^+p \rightarrow K^+\pi^-\pi^+p$ final state ($\cos\theta^H > 0$).

$\Delta(1910)$: $J^P = \frac{1}{2}^+$;

~25% branching ratio into $N\pi$,

$\Delta(1950)$: $J^P = \frac{7}{2}^+$;

~40% branching ratio into $N\pi$.

Also, the S_{31} wave (quoted mass 1650 MeV) has its maximum contribution to the πp elastic channel cross section around 1850 MeV; its contribution to our $\pi^+ p$ channel may be substantial.

In order to decide if the enhancement observed in Fig. 16 can be associated with any one of these states, its partial-wave content was explored. This was accomplished by investigation of the unnormalized $NH(LM)$ moments as a function of $p\pi^+$ mass (after a $\cos\theta^J > 0.0$ selection,²⁹ see above,

where

$$NH(LM) = \left(\frac{4\pi}{2L+1} \right)^{1/2} \sum Y_M^L(\theta_i, \phi_i)$$

and (θ_i, ϕ_i) correspond to the Jackson angles of the outgoing $p\pi^+$ system. The summation extends over all events in a given mass bin. The values of $NH(L0)$ for even L up to $L=8$ are shown in Figs. 17(a)–17(l) for the three reactions. Structure is observed in the region of the $\Delta(1880)$ enhancement for $H(L0)$ up to $L=6$, with no evidence for $L=8$. This implies that, if we are to attribute the observed signal to one resonant state, then it must have $J > \frac{1}{2} L = \frac{6}{2}$. Hence the most likely candidate is the $J^P = \frac{7}{2}^+ \Delta^{++}(1950)$.

Even though the statistics become marginal it

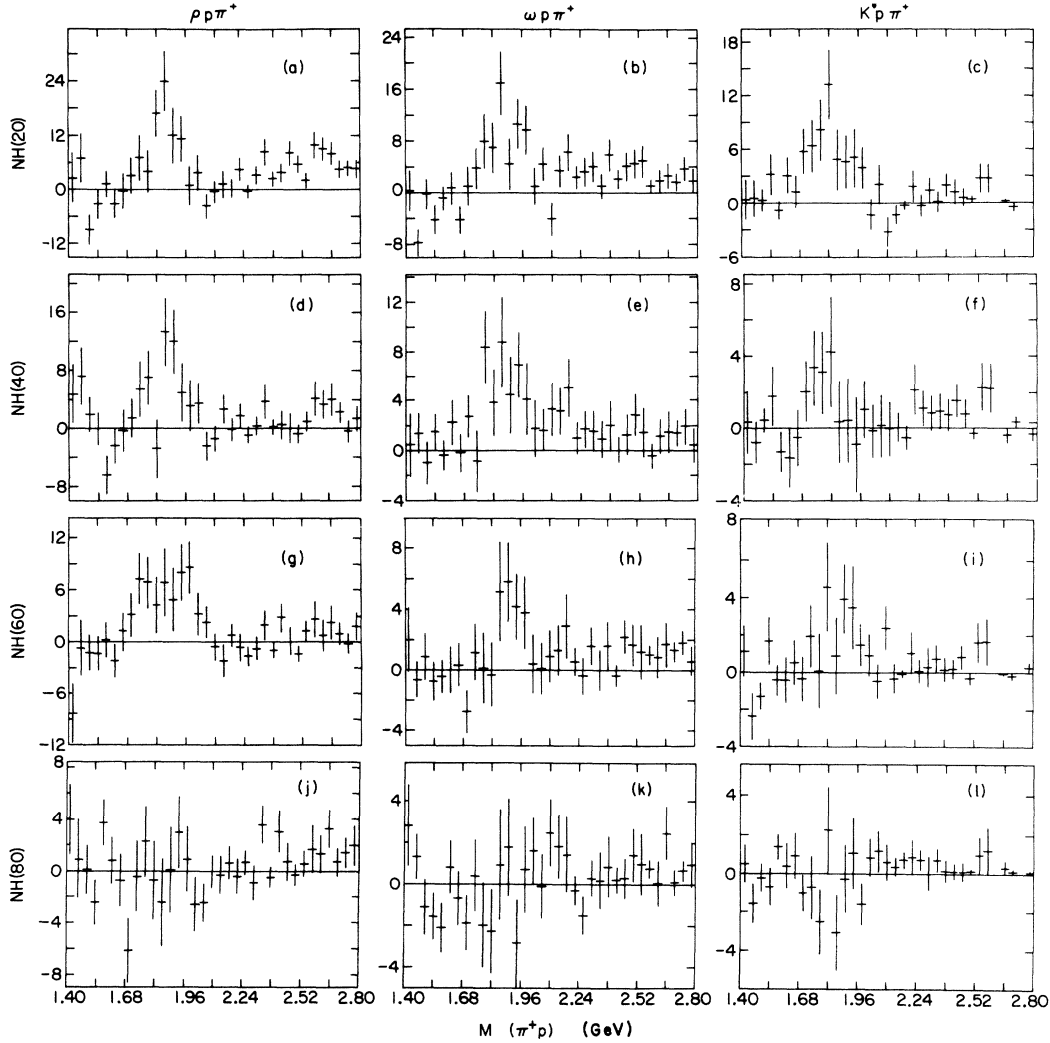


FIG. 17. (a), (d), (g), (j) Unnormalized moment $NH(L0)$ ($L=2, 4, 6, 8$, respectively) from the reaction $\pi^+ p \rightarrow \rho^0 \pi^+ p$. (b), (e), (h), (k) Same as (a), (d), (g), (j), but for the reaction $\pi^+ p \rightarrow \omega \pi^+ p$. (c), (f), (i), (l) Same as (a), (d), (g), (j), but for the reaction $K^+ p \rightarrow K^{*0}(890) \pi^+ p$

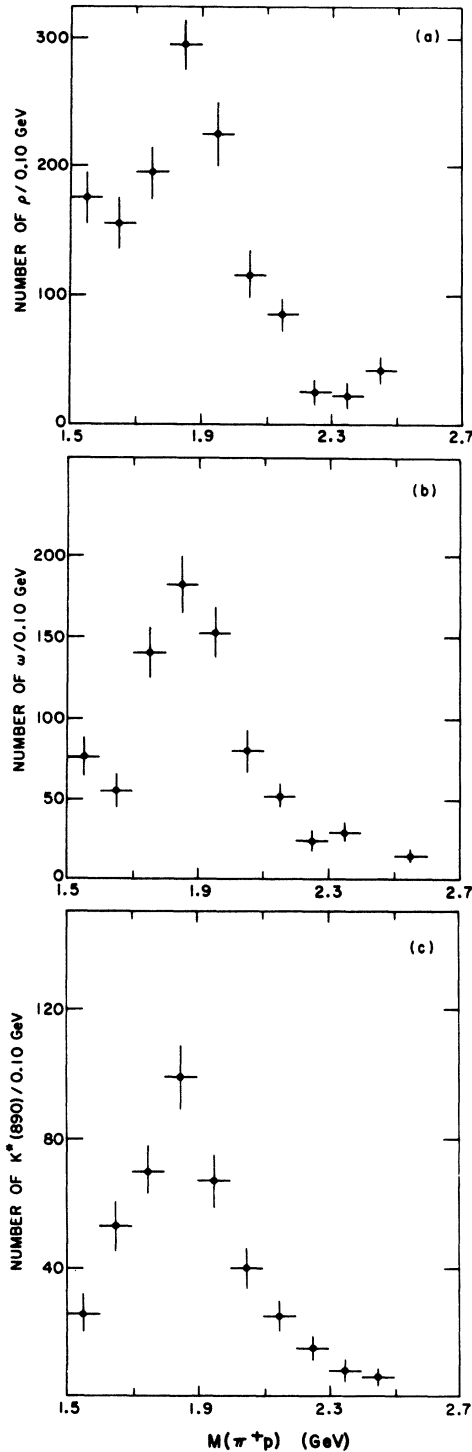


FIG. 18. Application of the slice technique: (a) Distribution of the number of ρ^0 events as a function of $p\pi^+$ effective mass for events with $\cos\theta^H > 0.0$ (see text) so as to eliminate the A_1 reflection under the $p\pi^+$ peak. (b) Same as (a), but for the ω final state. (c) Same as (a), but for the K^* final state.

does appear that the structure in the moments (see Fig. 17) has nearly the same mass and width as in the over-all mass spectra (see Fig. 16). Hence, the identification of a large portion of the bump primarily with one state and not with a series of different states with different J^P seems most likely.

Of interest to note is that, if the mass obtained from the phase-shift analyses is taken for the $J^P = \frac{1}{2}^+$ Δ state (i.e., 1930–1980 MeV), and if the same mass spacing as for the $J^P = \frac{3}{2}^+$ decuplet is assumed³⁰ (i.e., $\Delta m = m_\pi = 140$ MeV), then the Σ state is predicted to have a mass value of between 2070 and 2120 MeV. The $J^P = \frac{1}{2}^+$ $\Sigma(2030)$ has been determined⁹ to have a mass value of between 2020 and 2040 MeV. If we take the value of the mass of the Δ state determined here and again assume the same mass spacing as for the $\frac{3}{2}^+$ decuplet then we predict the Σ state to have mass (2021 ± 6) MeV, which better agrees with the experimentally determined value.

B. Production properties

1. Cross-section determination

The number of events of the reaction

$$\pi^+ p \rightarrow \rho^0 \Delta^{++} (1880) \quad (9)$$

$$- \omega \Delta^{++} (1880) \quad (10)$$

$$- K^* \Delta^{++} (1880) \quad (11)$$

was extracted with the slice technique described in Sec. III. For events with $\cos\theta^H > 0.0$ the distribution of the number of ρ , ω , and $K^*(890)$ events, obtained in each 100-MeV interval of $p\pi^+$ mass, is shown in Figs. 18(a)–18(c), respectively,³¹ in which large signals for $\Delta(1880)$ production are observed. The numbers of events in reactions (9)–(11) were extracted from these mass spectra from fits which included an S-wave Breit-Wigner resonance form (with mass and width fixed at 1880 MeV and 200 MeV, respectively) multiplying phase space and a second-order polynomial background term, and the following numbers of events were obtained:

$$\text{reaction (9)} = (617 \pm 45),$$

$$\text{reaction (10)} = (451 \pm 52),$$

$$\text{reaction (11)} = (224 \pm 32).$$

The cross sections were obtained under the assumption that the number of resonance events obtained with the $\cos\theta^H$ cut corresponded to one-half the total resonance cross section. This assumption is of course not valid in general if there is significant interference with background waves. After correction for unobserved neutral decays,

and for resonance tails, the cross sections corresponding to $\pm 4\Gamma$ (vector mesons) are³²

$$\text{reaction (9)} = (41 \pm 5) \mu\text{b},$$

$$\text{reaction (10)} = (26 \pm 3) \mu\text{b},$$

$$\text{reaction (11)} = (21 \pm 3) \mu\text{b}.$$

It should be emphasized, from an SU(3) point of view,²⁰ that production of $\Delta^{++}(1880)$ associated with both ρ ($G = -1$ exchange) and ω ($G = +1$ exchange) implies that $K^*(890) \Delta^{++}(1880)$ proceeds through both $G = +1$ and $G = -1$ exchange. This is contrary to the suggestion of Colley *et al.*,²⁸ who studied the K^* associated reaction at 10 GeV/ c and claimed it to be mediated almost entirely by a one-pion exchange mechanism.

2. $d\sigma/dt$

The differential cross section and $\rho_{mm'}$ of reactions (9)–(11) were extracted in a manner similar to that described in Sec. III. Here, the $\Delta^{++}(1880)$ mass slice was defined by

$$1.76 \leq M(p\pi^+) \leq 1.96 \text{ GeV},$$

a region which contains ~ 1 to 1 (~ 2 to 1) signal-to-noise with the associated ρ (ω) mass selection. This background has not been corrected for in the following discussion; however, an investigation of the vector-meson density matrix elements corresponding to $p\pi^+$ mass bands adjacent to the $\Delta^{++}(1880)$ region reveals no significant differences from the resonance region in the $|t|$ -dependent $\rho_{mm'}$ distributions. This provides ample justification for our neglect of the background, even though, with more statistics, it would be clearly desirable to obtain the true $\Delta^{++}(1880)$ + vector meson $\rho_{mm'}$ distributions free of back-

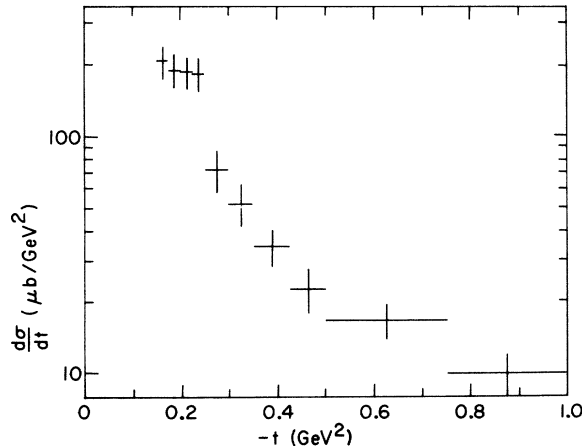


FIG. 19. $d\sigma/dt$ for the reaction $\pi^+p \rightarrow \rho^0\Delta^{++}(1880)$.

TABLE V. $d\sigma/dt$ vs t for reactions $\pi^+p \rightarrow \rho\Delta^{++}(1880)$, $\pi^+p \rightarrow \omega\Delta^{++}(1238)$.

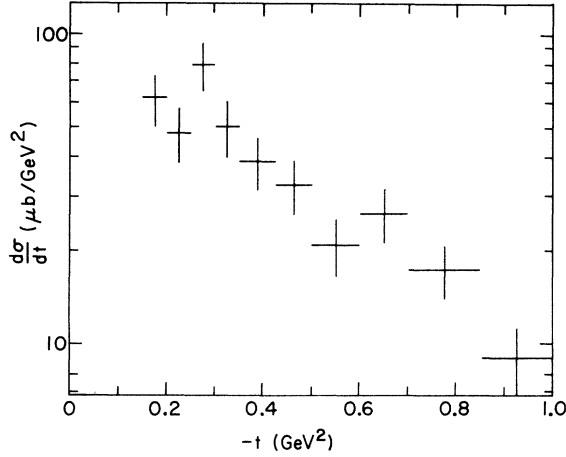
$-t$ bin (GeV ²)	No. of events	$d\sigma/dt$ ($\mu\text{b}/\text{GeV}^2$)
ρ		
0.150–0.175	68	207.1 \pm 33.2
0.175–0.200	62	188.9 \pm 31.
0.200–0.225	61	185.8 \pm 30.
0.225–0.250	60	182.8 \pm 30.
0.250–0.300	76	72.1 \pm 14.3
0.300–0.350	55	52.2 \pm 11.3
0.350–0.425	47	34.2 \pm 6.3
0.425–0.500	31	22.5 \pm 4.8
0.500–0.750	73	16.5 \pm 2.9
0.750–1.000	44	10.0 \pm 2.0
ω		
0.150–0.200	40	61.9 \pm 11.5
0.200–0.250	31	48.0 \pm 9.8
0.250–0.300	60	79.2 \pm 14.6
0.300–0.350	38	50.1 \pm 10.5
0.350–0.425	44	38.7 \pm 7.4
0.425–0.500	37	32.5 \pm 6.6
0.500–0.600	34	20.9 \pm 4.4
0.600–0.700	43	26.4 \pm 5.2
0.700–0.850	46	17.3 \pm 3.4
0.850–1.000	24	9.0 \pm 2.2

ground contamination.²⁹

With the above proviso, the differential cross section for reaction (9) [(10)] is shown in Fig. 19 (20) and is listed in Table V. The “ t_{\min} ” cutoff does not allow us to explore the very-low-momentum-transfer region. Like the $\Delta^{++}(1238)$ associated reactions, the $d\sigma/dt$ of the $\rho[\Delta(1880)]$ is observed to be markedly more peripheral than that of the $\omega[\Delta(1880)]$ reaction.

3. $\rho_{mm'}$

a. $\pi^+p \rightarrow \rho^0\Delta^{++}(1880)$. The $\rho_{mm'}^J$ ($\rho_{mm'}^H$) distributions are shown in Figs. 21(a)–21(c) [21(d)–21(f)] and are listed in Table VI. For $|t| < 0.3 \text{ GeV}^2$ the contribution of UNP exchange is apparent in the observed large values of ρ_{00} in both the t and s channels, with the former being larger in absolute magnitude. In the same momentum-transfer region $|\rho_{1-1}^H| > |\rho_{1-1}^J|$ and ρ_+ [Fig. 23(a)] is observed to be consistent with zero. Therefore, UNP entirely dominates the low- $|t|$ region. The helicity-one UNP components are shown in Fig. 23(b) (t channel, and Fig. 23(c) (s channel), and ρ_+^H is observed to be larger than the corresponding ρ_+^J . For $|t| > 0.5 \text{ GeV}^2$ $\rho_+ \approx 0.5$ and, as in $\rho^0\Delta^{++}(1238)$, NP exchanges becomes comparable to the total UNP.

FIG. 20. $d\sigma/dt$ for the reaction $\pi^+p \rightarrow \omega\Delta(1880)$.4. $\pi^+p \rightarrow \omega\Delta(1880)$

The ρ_{mm}^J , (ρ_{mm}^H) distributions are shown in Figs. 22(a)–22(c) [22(d)–22(f)] and are listed in Table VII. For $|t| < 0.35$ GeV², ρ_{00}^J and ρ_{00}^H are quite large, implying, as in $\omega\Delta^{++}(1238)$, a large helicity-zero UNP exchange contribution. For larger values of $|t|$ ρ_{00} is still sizable, with a value ≈ 0.4 in both frames. The errors in $\rho_{1-1}^{J,H}$ are large. Its values show some deviation from, but are consistent with, zero in the momentum-transfer region of interest. ρ_+ [Fig. 24(a)] is, as for $\rho\Delta(1880)$, consistent with zero for $|t| < 0.35$ GeV², and increases at larger values of $|t|$. The errors in the values of ρ_-^J (ρ_-^H) are too large to allow any strong conclusions as to the behavior of UNP helicity one. However, as seen in Fig. 24(b) [24(c)], the distribution shows nonzero values in

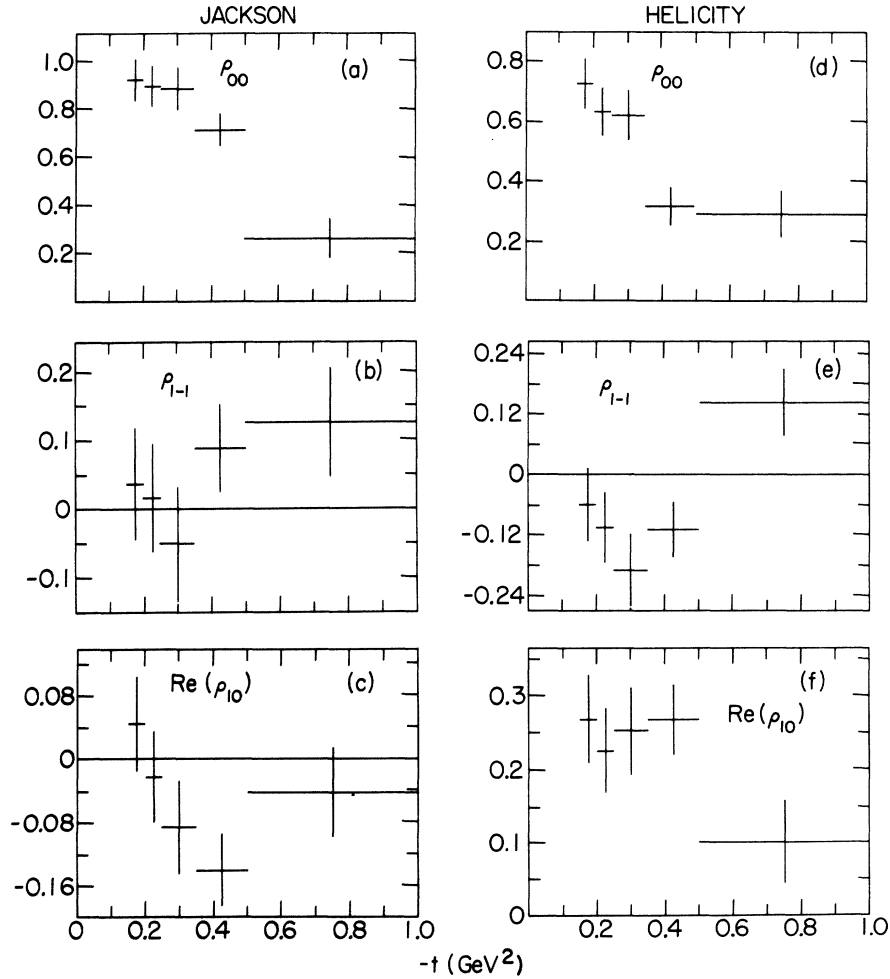


FIG. 21. (a) Distribution of ρ_{00}^J for the ρ^0 as a function of $-t$ from the reaction $\pi^+p \rightarrow \rho^0\Delta(1880)$. (b) Distribution of ρ_{1-1}^J . (c) Distribution of $\text{Re}\rho_{10}^J$. (d) Same as (a), but for ρ_{00}^H . (e) Same as (b), but for ρ_{1-1}^H . (f) Same as (c), but for $\text{Re}\rho_{10}^H$.

TABLE VI. Density-matrix elements vs t for reaction $\pi^+p \rightarrow \rho\Delta^{++}(1880)$.

$-t$ bin (GeV ²)	No. of events	Fraction	Jackson frame			Helicity frame		
			ρ_{00}	ρ_{1-1}	$\text{Re}(\rho_{10})$	ρ_{00}	ρ_{1-1}	$\text{Re}(\rho_{10})$
0.150-0.200	130	1.000 ± 0.105	0.919 ± 0.086	0.036 ± 0.082	0.044 ± 0.059	0.726 ± 0.083	-0.061 ± 0.072	0.268 ± 0.060
0.200-0.250	121	1.000 ± 0.102	0.893 ± 0.083	0.016 ± 0.079	-0.022 ± 0.057	0.634 ± 0.080	-0.106 ± 0.069	0.225 ± 0.058
0.250-0.350	131	0.623 ± 0.106	0.883 ± 0.087	-0.051 ± 0.083	-0.086 ± 0.059	0.619 ± 0.084	-0.190 ± 0.072	0.252 ± 0.060
0.350-0.500	78	0.716 ± 0.082	0.711 ± 0.067	0.088 ± 0.064	-0.141 ± 0.046	0.315 ± 0.065	-0.109 ± 0.056	0.267 ± 0.047
0.500-1.000	117	0.743 ± 0.100	0.258 ± 0.082	0.125 ± 0.078	-0.042 ± 0.056	0.290 ± 0.079	0.142 ± 0.068	0.101 ± 0.057

the momentum-transfer region examined.

Therefore, for both the $\rho\Delta(1880)$ and $\omega\Delta(1880)$ reactions, UNP exchange dominates, especially in the smaller-momentum-transfer region.

VI. COMPARISON OF $(\rho,\omega)\Delta^{++}(1238)$ AND $(\rho,\omega)\Delta^{++}(1880)$

As noted above, the properties of the $\Delta^{++}(1238)$ + vector meson are qualitatively similar to those of $\Delta^{++}(1880)$ + vector meson reactions. In all reactions UNP dominates, with the π -exchange (ρ =vector meson) reactions more peripheral than the corresponding B -exchange (ω =vector meson) processes.

In order to quantitatively compare the reactions the observables are now compared in the different reaction sets. In Fig. 25(a) is shown the ratio, $\Delta^{++}(1880)/\Delta^{++}(1238)$, of the differential cross section for the ρ^0 reactions. Figure 25(b) shows a similar ratio, but for the associated ω reactions. In the ρ^0 reaction, disregarding the obvious ≈ 2 -standard-deviation fluctuation (see Fig. 19) in the 0.20-0.25 GeV² $|t|$ interval of $\rho\Delta(1880)$, the ratio of the two $d\sigma/dt$'s is constant as a function of $|t|$ with an observed value of ~ 0.22 . For the ω reactions, the ratio for $|t| \lesssim 0.6$ is consistent with a constant whose value is close to that found in the ρ set. The statistics are not good enough, however, to rule out a rise with momentum transfer in this ratio. For larger values of $|t|$ the relative $\Delta(1880)$ -to- $\Delta(1238)$ ratio is observed to increase to a value of ~ 0.7 .

We look more closely at the exchange contributions in these reactions and plot in Fig. 26 the relative ratio of the dominant UNP ($\rho_{00} + \rho_{-} = 1 - \rho_{+}$) exchange in the $\Delta(1880)$ and $\Delta(1236)$ reactions. The fine $|t|$ -dependent details observed between the ρ and ω sets are somewhat different but both show a relative increase in going from $\Delta^{++}(1236)$ to $\Delta^{++}(1880)$.

We pursue this approach and remark that Hoyer, Roberts, and Roy³³ have related through finite-mass sum rules the low-mass resonance region and the triple-Regge region for processes of the type $a + b \rightarrow c + X$. For the specific case of interest, $\pi^+p \rightarrow$ vector meson + X , their approach leads to the expectation that the average resonance cross section (i.e., with mass $M=M_x$) due to Reggeon exchange has the behavior

$$\sigma_X \sim (M_x^2)^{\alpha_M(0) - 2\alpha_R(t)},$$

where $\alpha_M(0)$ is the intercept of the Reggeon coupling to $p\bar{p}$ and $\alpha_R(t)$ is the Regge trajectory which couples to $\pi^+\rho^0$ ($\sim \pi^+\omega$). This leads to the expectation, based upon the assumption that

$$\alpha_{\text{UNP}}(t) = \alpha_{\pi}(t) = \alpha_{\text{B}}(t) = 0.0 + t$$

and

$$\alpha_{\text{NP}}(t) = \alpha_{\rho}(t) = \alpha_{\text{A}_2}(t) = 0.5 + t,$$

that

$$\frac{\sigma_{\text{NP}}}{\sigma_{\text{UNP}}} \propto \frac{1}{M_X^2} \quad (12)$$

at fixed s and t . That is, the relative NP/UNP cross section should decrease with increasing mass.

In Fig. 27(a) [27(b)] is shown the NP/UNP ratio for the $\rho\Delta(1238)$ [$\Delta(1880)$] and $\omega\Delta(1238)$ [$\Delta(1880)$] sets. We immediately observe that, within the rather large errors, both the ω and the ρ data are in agreement with (12) since this ratio is smallest for the larger mass resonance. The solid curve in Fig. 27(a) [27(b)] is an eyeball "fit" to the $\rho(\omega)\Delta^{++}(1238)$ data. The dashed curve rep-

resents the predicted NP/UNP fraction derived from the corresponding solid curve scaled by a factor M_{1238}^2/M_{1880}^2 as dictated by (12). This curve is in remarkably good agreement with the trend of the data; however, the large errors in the $\Delta^{++}(1880)$ sets added to our inability to adequately take into account the background under the $p\pi^+$ enhancement in our determination of the ρ_{mm} , do not allow us to be more quantitative. The result is in agreement with that found in a study³³ of the reaction $\pi^-p \rightarrow (\rho, f^0, g)m$ in which $\sigma_{\text{NP}}/\sigma_{\text{UNP}}$ has been found to decrease similarly with increasing resonance mass.

VII. SUMMARY AND CONCLUSIONS

From a large sample of events of the reactions $\pi^+p \rightarrow (\rho, \omega)\Delta^{++}(1238)$ a systematic analysis has yielded cross-section, differential-cross-section, and vector-meson single density-matrix ele-

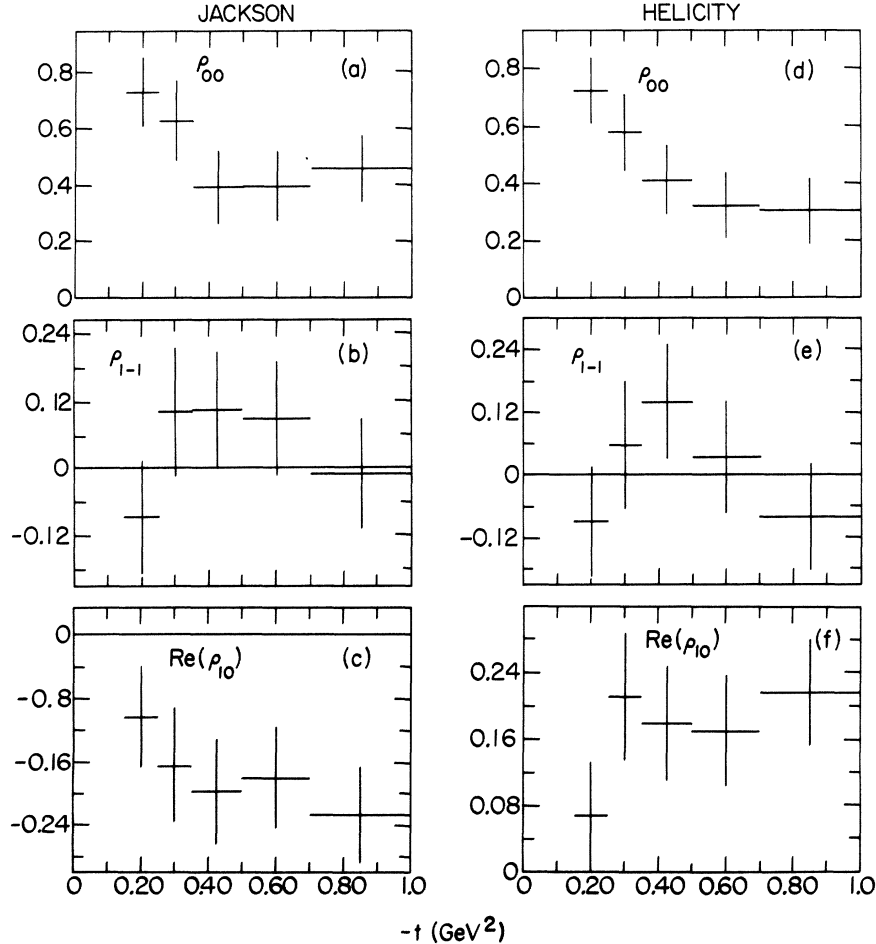


FIG. 22. (a) Distribution of ρ_{00}^f for the ω as a function of $-t$ from the reaction $\pi^+p \rightarrow \omega\Delta(1880)$. (b) Distribution of ρ_{1-1}^f . (c) Distribution of $\text{Re}\rho_{10}^f$. (d) Same as (a), but for ρ_{00}^H . (e) Same as (b), but for ρ_{1-1}^H . (f) Same as (c), but for $\text{Re}\rho_{10}^H$.

TABLE VII. Density-matrix elements vs t for reaction $\pi^+p \rightarrow \omega\Delta^{++}(1880)$.

$-t$ bin (GeV ²)	No. of events	Fraction	Jackson frame			Helicity frame		
			ρ_{00}	ρ_{1-1}	$\text{Re}(\rho_{10})$	ρ_{00}	ρ_{1-1}	$\text{Re}(\rho_{10})$
0.150-0.250	71	1.000 ± 0.098	0.727 ± 0.122	-0.086 ± 0.100	-0.103 ± 0.064	0.723 ± 0.115	-0.090 ± 0.105	0.068 ± 0.065
0.250-0.350	98	0.853 ± 0.112	0.624 ± 0.141	0.101 ± 0.115	-0.165 ± 0.073	0.577 ± 0.133	0.057 ± 0.121	0.211 ± 0.075
0.350-0.500	81	0.852 ± 0.102	0.391 ± 0.128	0.104 ± 0.104	-0.198 ± 0.067	0.410 ± 0.120	0.139 ± 0.110	0.179 ± 0.068
0.500-0.700	77	0.793 ± 0.100	0.394 ± 0.125	0.088 ± 0.102	-0.181 ± 0.065	0.320 ± 0.117	0.034 ± 0.107	0.170 ± 0.066
0.700-1.000	70	0.730 ± 0.095	0.456 ± 0.119	-0.010 ± 0.097	-0.227 ± 0.062	0.304 ± 0.112	-0.082 ± 0.102	0.216 ± 0.063

ments. No significant structures, as previously claimed,¹⁶ are observed in the appropriate distributions which would correspond to wrong-signature nonsense zeros of π , B , or ρ Regge poles. The large forward peak in $\rho_{00} d\sigma/dt$ in the $\rho\Delta$ reaction corresponding to the π -exchange contribution to the $n=0$ amplitude has been investigated. A small but significant natural-parity component is observed at small $|t|$. In $\omega\Delta^{++}$

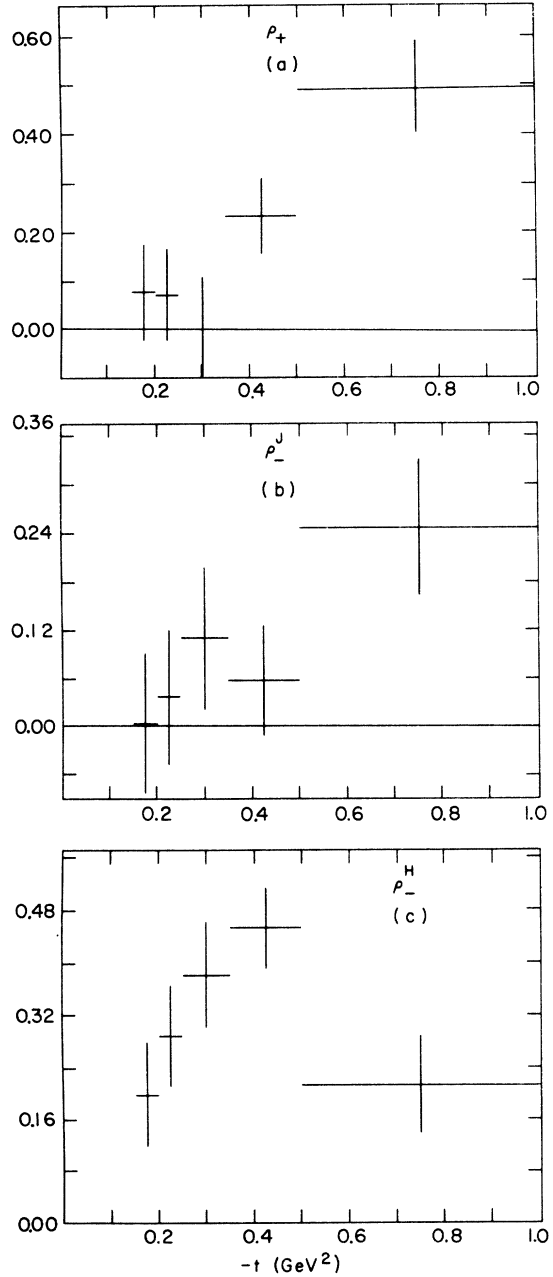


FIG. 23. (a) ρ_+ for the ρ^0 from the reaction $\pi^+p \rightarrow \rho^0\Delta(1880)$. (b) Same as (a), but for ρ_-^J . (c) Same as (a), but for ρ_-^H .

sizeable UNP exchange has been observed. The $\rho\Delta/\omega\Delta$ relative cross section ratio as a function of $-t$ is determined here to be larger than in previous experiments¹⁶ in this energy region. The possibility that the discrepancy results from the method of cross-section extraction has been suggested.

In addition, data have been presented with strong

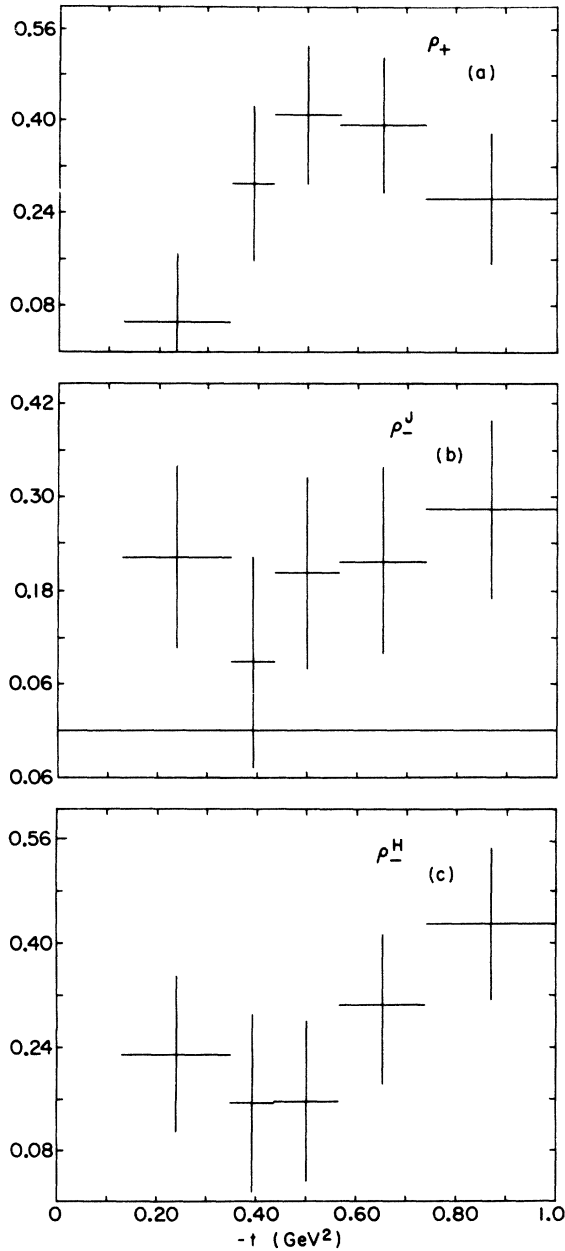


FIG. 24. (a) ρ_+ for the ω from the reaction $\pi^+p \rightarrow \omega\Delta$ (1880). (b) Same as (a), but for ρ_-^J . (c) Same as (a), but for ρ_-^H .

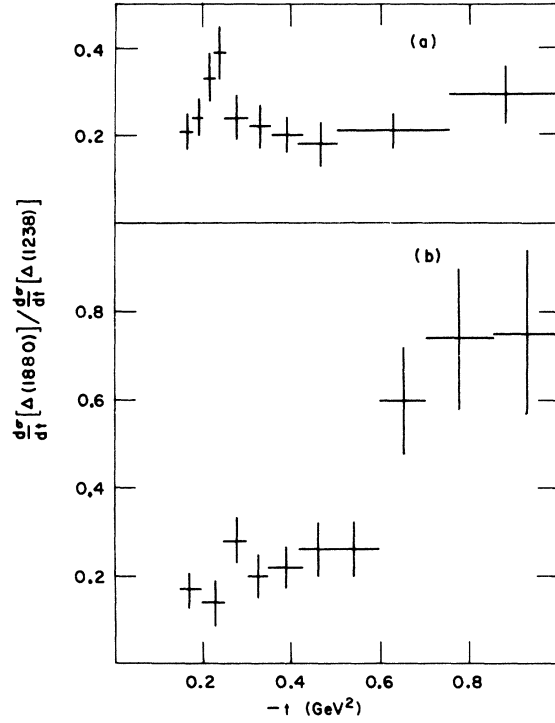


FIG. 25. (a) Ratio of the differential cross sections: $d^2\sigma/dt^2[\rho^0\Delta^{++}(1880)]/d^2\sigma/dt^2[\rho^0\Delta^{++}(1238)]$. (b) Same as (a), but for the corresponding ω reactions.

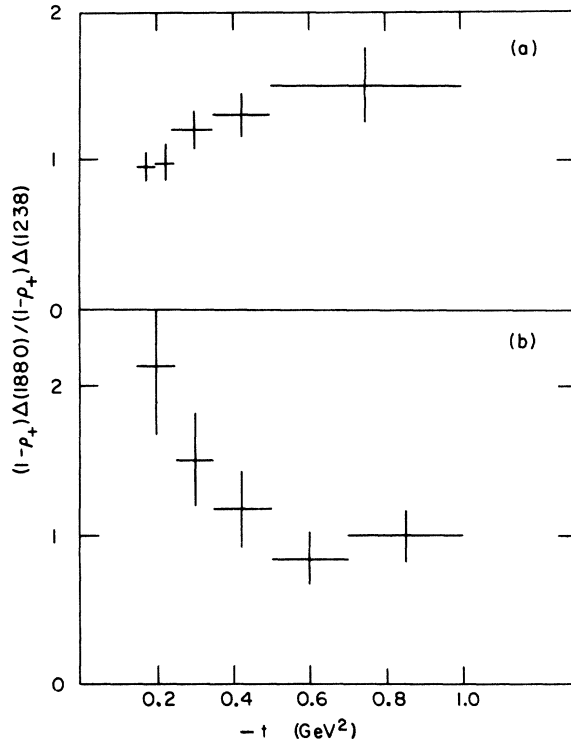


FIG. 26. (a) Ratio of the UNP contributions: $(1-\rho_+)\Delta(1880)/(1-\rho_+)\Delta(1238)$. (b) Same as (a), but for the corresponding ω reactions.

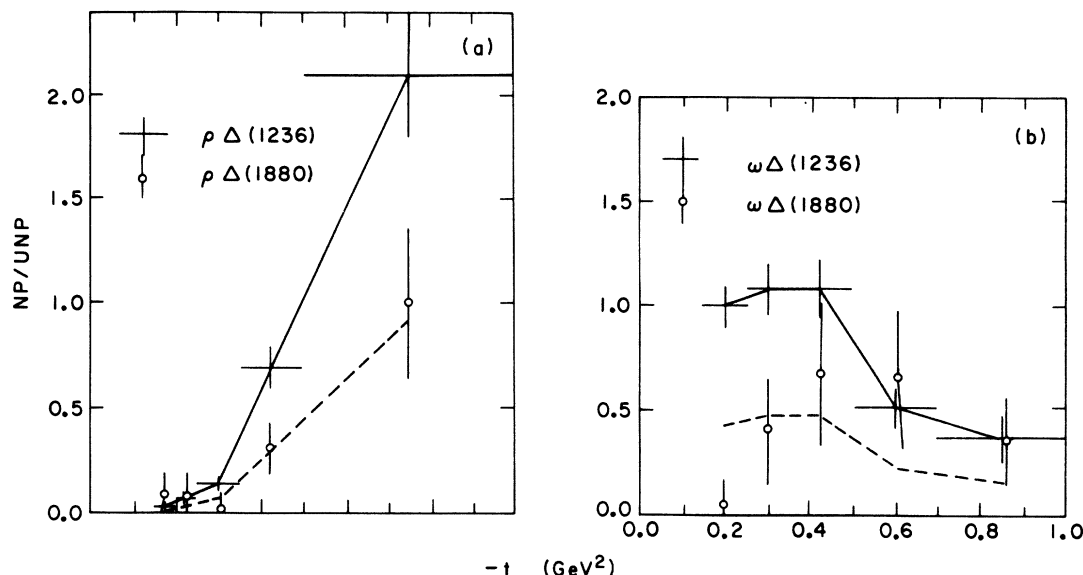


FIG. 27. (a) (Natural-parity)/(Unnatural-parity) fractions for $\rho \Delta^{++}(1880)$ compared to $\rho^0 \Delta^{++}(1238)$. (b) Same as (a), but for the corresponding ω reactions. The solid lines represent "eyeball" fits to the ρ (ω) $\Delta^{++}(1238)$ ratio. The dashed curves represent "predictions" for the corresponding ρ (ω) $\Delta^{++}(1880)$ reaction.

evidence for the production of a high-mass $p\pi^+$ state with $M=(1881.2 \pm 5.5)\text{MeV}$ and $\Gamma=(219 \pm 23)\text{MeV}$ with a most probable $J^P = \frac{1}{2}^+$ assignment corresponding to the $\Delta^{++}(1950)$ observed in πp phase-shift analyses. The state is produced in association with the ρ and ω resonances, so that π exchange alone cannot be the only exchange contribution to the production in the reaction $K^+ p \rightarrow K^*(890) \Delta^{++}(1880)$, which we also observe. In agreement with theoretical predictions, the UNP-to-NP fraction appears to be larger in the $\pi^+ p \rightarrow (\omega, \rho) \Delta^{++}(1880)$ reaction than in the $\pi^+ p \rightarrow (\omega, \rho) \Delta^{++}(1238)$ reaction.

ACKNOWLEDGMENTS

We thank Dr. J. Owens for his many valuable comments and suggestions. One of us (R. L. E.) would like to acknowledge the support and encouragement of Dr. W. Fickinger and Dr. D. K. Robinson. S. U. C. and S. D. P. acknowledge the support of Dr. N. P. Samios. We thank members of Lawrence Berkeley Laboratory Group A, in particular Dr. M. Alston-Garnjost, Dr. A. Barbaro-Galtieri, Dr. G. Lynch, and Dr. F. T. Solmitz, for providing us with the data for this analysis.

*Work performed under the auspices of the U. S. Energy Research and Development Administration.

†Work supported by the National Science Foundation.

¹S. D. Protopopescu, M. Alston-Garnjost, A. Barbaro-Galtieri, S. M. Flatté, J. H. Friedman, T. A. Lasinski, G. R. Lynch, M. S. Rabin, and F. T. Solmitz, Phys. Rev. D **7**, 1279 (1973).

²W. F. Buhl, G. Gidal, D. F. Grether, W. Ko, M. Alston-Garnjost, A. Barbaro-Galtieri, G. R. Lynch, and F. T. Solmitz, Phys. Lett. **49B**, 388 (1974).

³P. J. Davis, M. Alston-Garnjost, A. Barbaro-Galtieri, S. M. Flatté, J. H. Friedman, G. R. Lynch, M. S. Rabin, and F. T. Solmitz, Phys. Rev. D **5**, 2688 (1972).

⁴M. Aguilar-Benitez, S. U. Chung, R. L. Eisner, and N. P. Samios, Phys. Rev. D **6**, 29 (1972).

⁵A mass of 780 MeV and width of 174 MeV were obtained for the ρ^0 . We have not included a more sophisticated background parametrization and obtained the best es-

timate of these values, which would result from a fit to a larger portion of the $\pi^+\pi^-$ mass spectrum.

⁶In the region of the fit, the background parametrization and relative ρ signal to nonresonant $\pi^+\pi^-$ agree well with those obtained from the $\pi\pi$ phase-shift analysis of Ref. 1.

⁷The theoretical P -wave form was extrapolated into the resonance wings and gives the quoted scale factor. This corresponds to the ratio

$$\frac{M\rho \pm 4\Gamma\rho}{\text{fitted region} = 0.40 \leq M(\pi^+\pi^-) \leq 0.82 \text{ GeV}}$$

⁸The quoted error is only statistical and hence does not include systematic uncertainties in the background parametrization.

⁹For a complete set of references see Particle Data Group, Phys. Lett. **50B**, 1 (1974).

¹⁰M. Aguilar-Benitez, S. U. Chung, and R. L. Eisner, Phys. Rev. D 6, 11 (1972).

¹¹The approach was justified from an examination of the angular dependence in $\pi^+\pi^-\pi^0$ mass bands adjacent to the ω region which revealed no significant correlations.

¹²The maximum value of $|t_{\min}|$ corresponding to the Δ^{++} and $\rho(\omega)$ resonance regions is $\sim 0.05 \text{ GeV}^2$. The $d\sigma/dt$ distribution will tend to be artificially lowered below this value of momentum transfer.

¹³For a complete set of references on determination of ρ_{mm^*} at other beam momenta for reaction $\pi^+p \rightarrow \rho(\omega)\Delta^{++}$, see J. A. Gaidos *et al.*, Nucl. Phys. B72, 253 (1974).

¹⁴See, for example the discussion by G. Ciapetti *et al.*, Nucl. Phys. B64, 58 (1973).

¹⁵See also R. D. Field and D. P. Sidhu, Phys. Rev. D 10, 89 (1974).

¹⁶G. S. Abrams, K. W. J. Barnham, W. R. Butler, D. G. Coyne, G. Goldhaber, B. H. Hall, and J. McNaughton, Phys. Rev. Lett. 25, 617 (1970).

¹⁷A. C. Irving and C. Michael, CERN Report No. TH. 1525, 1974 (unpublished).

¹⁸As, for example, proposed by T. Ferbel, P. Slattery, and B. Werner, Phys. Rev. Lett. 26, 344 (1971).

¹⁹G. S. Abrams and U. Maor, Phys. Rev. Lett. 25, 621 (1970).

²⁰As shown by G. Ciapetti, R. L. Eisner, A. C. Irving, J. B. Kinson, and D. C. Watkins [Nucl. Phys. B66, 1350 (1973)], data show that

$$\frac{1}{2} \left[\rho_{00}^J \frac{d\sigma}{dt} (\pi^+p \rightarrow \rho^0\Delta^{++}) + \rho_{00}^J \frac{d\sigma}{dt} (\pi^+p \rightarrow \omega\Delta^{++}) \right] \\ = \rho_{00}^J \frac{d\sigma}{dt} (K^+p \rightarrow K^{*0}\Delta^{++}),$$

a result in agreement with weakly EXD π - B Regge poles.

²¹The same result as found in Ref. 20, but using the data of the present work, has been found by R. L. Eisner, J. Owens, S. U. Chung, and S. Protopopescu (unpublished).

²²Relationships similar to that in Ref. 20 can be derived under the interchange $\Delta^{++} \rightarrow$ nucleon. The weak EXD scheme also works, as shown in Ref. 20 and in Ref. 14.

²³P. Estabrooks and A. D. Martin, Phys. Lett. 41B, 350 (1972).

²⁴C. Michael, Nucl. Phys. B63, 431 (1973).

²⁵For preliminary results on the π^+p enhancement at 1.880 GeV, see S. U. Chung *et al.*, (unpublished).

²⁶Actually, the contamination is much smaller in the $\pi^+p \rightarrow \omega\pi^+p$ reaction; however, in order to treat all samples in a consistent fashion the $\cos\theta^H$ selection was imposed. This selection does improve the resonance signal-to-noise ratio in this sample.

²⁷We used an s -wave (rather than f -wave) Breit-Wigner shape because there is as yet no general agreement on how to parametrize a resonance with nonzero orbital angular momentum. At this high mass an s -wave Breit-Wigner shape is probably as good a parametrization as any other, and our statistics are not high enough to warrant a detailed study of this problem. Our quoted errors on Γ and M are statistical only and do not take into account possible shifts due to changes in parametrization.

²⁸D. C. Colley, S. S. Huq, M. Jobes, J. B. Kinson, J. Milne, P. M. Watkins, I. S. Hughes, J. McCormick, and R. M. Turnbull, Nucl. Phys. B69, 205 (1974).

²⁹In order to make statements pertaining to a resonant state, a freely (no interference) decaying particle hypothesis is assumed, at least for resonance events produced away from the low-mass enhancements.

³⁰See the fits by N. P. Samios, M. Goldberg, and B. T. Meadows, Rev. Mod. Phys. 46, 49 (1974).

³¹The resonance regions were defined as follows: $\rho = 0.4 < M(\pi^+\pi^-) \leq 1.0 \text{ GeV}$, $\omega = 0.68 < M(\pi^+\pi^-\pi^0) \leq 0.88 \text{ GeV}$, $K^* = 0.70 < M(K^+\pi^-) \leq 1.1 \text{ GeV}$.

³²A correction is needed only for ρ^0 events. See Ref. 31 for the region of fit.

³³P. Hoyer, R. G. Roberts, and D. P. Roy, Nucl. Phys. B56, 173 (1973); see also Ref. 24.